

Tumour-derived small extracellular vesicles act as a barrier to therapeutic nanoparticle delivery

Received: 23 January 2023

Accepted: 25 June 2024

Published online: 02 September 2024

 Check for updates

Ningqiang Gong^{1,2,13}, Wenqun Zhong^{3,13}, Mohamad-Gabriel Alameh^{4,13}, Xuexiang Han¹, Lulu Xue¹, Rakan El-Mayta¹, Gan Zhao⁵, Andrew E. Vaughan⁵, Zhiyuan Qin³, Fengyuan Xu³, Alex G. Hamilton¹, Dongyoon Kim¹, Junchao Xu¹, Junhyong Kim³, Xucong Teng⁶, Jinghong Li⁶, Xing-Jie Liang⁷, Drew Weissman^{4,8}, Wei Guo³ & Michael J. Mitchell^{1,8,9,10,11,12}

Nanoparticles are promising for drug delivery applications, with several clinically approved products. However, attaining high nanoparticle accumulation in solid tumours remains challenging. Here we show that tumour cell-derived small extracellular vesicles (sEVs) block nanoparticle delivery to tumours, unveiling another barrier to nanoparticle-based tumour therapy. Tumour cells secrete large amounts of sEVs in the tumour microenvironment, which then bind to nanoparticles entering tumour tissue and traffic them to liver Kupffer cells for degradation. Knockdown of *Rab27a*, a gene that controls sEV secretion, decreases sEV levels and improves nanoparticle accumulation in tumour tissue. The therapeutic efficacy of messenger RNAs encoding tumour suppressing and pro-inflammatory proteins is greatly improved when co-encapsulated with *Rab27a* small interfering RNA in lipid nanoparticles. Together, our results demonstrate that tumour cell-derived sEVs act as a defence system against nanoparticle tumour delivery and that this system may be a potential target for improving nanoparticle-based tumour therapies.

Nanoparticle-based tumour drug delivery systems have shown great promise for disease treatment in the clinic^{1,2}. It is desired that nanoparticles deliver drugs and genes specifically to tumour tissues for tumour cell killing or tumour microenvironment modulation³. However, studies have shown that only 0.7% of injected nanoparticles can reach solid tumours⁴. To improve delivery efficiency, several strategies have been developed. For example, studies focused on the optimization of the size⁵, shape⁶, surface chemistry⁷ and stiffness⁸ of nanoparticles to improve tumour accumulation through the passive mechanism of enhanced permeability and retention⁹ or through the active mechanism of ligand-based targeting¹⁰. Others have demonstrated that the protein corona on nanoparticles can alter their tumour accumulation^{11,12}.

In addition, reduced hepatic clearance of nanoparticles can improve their blood circulation and enhance tumour accumulation¹³. Although these strategies have demonstrated promise, improved nanoparticle accumulation in tumour tissues remains marginal, limiting the potential of nanoparticles for tumour treatment.

Recent studies have found that the dense extracellular matrix¹⁴, solid stress¹⁵ and abnormal vascular structures^{9,16,17} in the tumour microenvironment¹⁸ are critical factors that may affect nanoparticle tumour accumulation¹⁹, and these have been taken into consideration in improving nanoparticle design for tumour accumulation²⁰. The high level of small extracellular vesicles (sEVs) in solid tumours²¹ is an understudied factor that may affect nanoparticle accumulation,

as the high sEV gradient between tumours and healthy tissue²² may act as a biological barrier for nanoparticle penetration and accumulation.

Here, we found that tumour cell-derived sEVs act as a defence system against nanoparticle tumour delivery and that overcoming this intrinsic defence mechanism can improve the delivery of therapeutic nanoparticles to tumours and improve tumour treatment.

Rab27a knockout promotes nanoparticle accumulation in tumours

Studies have shown that there are high concentrations of sEVs in many solid tumours^{22,23}, with malignant cells representing the major source of sEVs²³ and *Rab27a* as a major gene that controls sEV secretion²⁴. We first induced *Rab27a* knockout (KO) using the clustered regularly interspaced short palindromic repeats (CRISPR)–Cas9 system in a mouse colon tumour cell line, MC38 (MC38 *Rab27a* KO) and a mouse melanoma cell line, YUMML7 (YUMML7 *Rab27a* KO). Tumour models were constructed using wild-type (WT) or KO cells. We found that *Rab27a* KO decreased tumour growth in immune competent mice²⁵. This is because sEVs can suppress anti-tumour immunity^{25–31}. Since we wanted to compare nanoparticle accumulation in WT and *Rab27a* KO tumours with similar tumour volumes, we depleted CD8⁺ T cells³² to ensure that tumour growth is not affected by *Rab27a* KO. Lipid nanoparticles (LNPs) were used as a model nanoparticle in this article³³. LNPs were labelled with a fluorescent dye (1,1'-dioctadecyl-3,3',3'-tetramethylindotricarbocyanine iodide (DiR)) and intravenously (i.v.) administered. After 24 h, mouse organs and tumours were collected and in vivo imaging system (IVIS), flow cytometry and immunofluorescence experiments were performed to examine LNP biodistribution in both the MC38 (Fig. 1 and Supplementary Figs. 1–6) and the YUMML7 tumour models (Supplementary Figs. 7–11). As expected, WT tumour-bearing mice displayed a typical distribution pattern in the liver and spleen with negligible fluorescence detected in the tumour (Fig. 1a and Supplementary Fig. 7a). In contrast, *Rab27a* KO tumour-bearing mice with CD8⁺ T cell depletion showed significant increases in DiR signal in the tumour tissue compared with WT tumour-bearing mice treated with LNP (Fig. 1b–d and Supplementary Fig. 7b–d). A slightly decreased DiR signal was observed in the livers of mice bearing *Rab27a* KO tumours compared with that of the WT tumour-bearing mice (Fig. 1b and Supplementary Fig. 7b). We also demonstrated that the observed nanoparticle accumulation in *Rab27a* KO tumours was not a result of CD8⁺ T cell depletion (Supplementary Fig. 2). Instead, *Rab27a* KO led to increased LNP delivery to tumours. Through flow cytometry experiments (Fig. 1e–h and Supplementary Figs. 3–5, 7e–g, 8 and 9), we found that LNP accumulation in liver Kupffer cells was significantly decreased in *Rab27a* KO tumour-bearing mice compared with WT tumour-bearing mice. However, LNP biodistribution in CD31⁺ endothelial cells, CD19⁺ B cells and hepatocytes remained unaffected (Supplementary Fig. 1e–g and Supplementary Fig. 8a–d). We also analysed LNP biodistribution in both blood and spleen and found no difference between WT and *Rab27a* KO tumour-bearing mice (Supplementary Figs. 3, 4, 8e–h and 9a–c). However, *Rab27a* KO greatly increased LNP uptake by tumour cells and tumour-infiltrating immune cells (Fig. 1h and Supplementary Figs. 5 and 9d–h). Collectively, these results indicate that inhibition of sEV secretion by *Rab27a* KO substantially increased LNP uptake by cells in tumours and simultaneously decreased uptake by Kupffer cells.

We further investigated the biodistribution of LNPs in WT or *Rab27a* KO MC38 and YUMML7 tumour-bearing Ai14 mice that possess a loxP-Stop-loxP-tdTomato expression cassette (Fig. 1i,j and Supplementary Figs. 6, 10 and 11). Cre recombinase messenger RNA (Cre mRNA) encapsulated in LNPs was used for the biodistribution assay. We found that the majority of LNPs accumulated in liver hepatocytes (Fig. 1i,j and Supplementary Figs. 6 and 10). In the livers of WT tumour-bearing mice, there was also high LNP uptake by Kupffer cells (Fig. 1i and Supplementary Fig. 10). However, in the *Rab27a* KO tumour-bearing mice, LNP uptake by Kupffer cells was decreased

(Fig. 1i,j and Supplementary Fig. 10a). We also found that LNP accumulation in *Rab27a* KO tumour tissues was notably higher than that of WT tumour tissues (Fig. 1k,l and Supplementary Fig. 11). We repeated the IVIS imaging experiment and found that the biodistribution pattern of LNPs at 24 and 48 h post injection did not change (Supplementary Fig. 12), further confirming that *Rab27a* KO affected LNP biodistribution. We also demonstrated that liver enzyme levels across different groups were similar (Supplementary Fig. 13), indicating that the altered liver biodistribution was not a result of differences in liver damage among the different groups. Altogether, *Rab27a* KO in tumour cells decreased LNP uptake by Kupffer cells and enhanced LNP delivery to tumour cells.

sEV binding to LNPs drives trafficking to liver Kupffer cells

In vivo biodistribution experiments demonstrated that sEV levels in tumour tissue affect LNP accumulation in tumours (Fig. 1k,l, Supplementary Fig. 11). We then sought to investigate the possible mechanism underlying this. We first demonstrated that tumour sEVs did not affect the phagocytic capability of Kupffer cells, as the cells express similar levels of the phagocytosis marker CD206 in different groups (ref. 34) (Fig. 2a,b). We then explored whether sEVs affect LNP uptake by Kupffer cells (Supplementary Fig. 14). We found that sEVs were taken up specifically by Kupffer cells while LNP uptake by Kupffer cells was lower (Supplementary Fig. 14b). However, mixing LNPs with sEVs before incubation with cells greatly increased LNP uptake by Kupffer cells (Fig. 2c,d), indicating that there might be physical interactions between sEVs and LNPs. Using transmission electron microscopy (TEM) (Fig. 2e,f and Supplementary Fig. 15a,b) and a pull-down assay (Fig. 2g and Supplementary Fig. 15c–e), we demonstrated the presence of physical interactions between LNPs and sEVs. Van der Waals interactions between sEVs and LNPs may be responsible for the interactions between the two particles³⁵.

The uptake of sEVs by cells relies on sEV surface adhesion molecules³⁶. Since we have demonstrated that there are physical interactions between sEVs and LNPs, it is possible that the uptake of LNPs by Kupffer cells is mediated by certain surface molecules on sEVs. Thus, we used antibodies to block adhesion molecules on sEVs to investigate their effects on the cellular uptake of LNPs by Kupffer cells. We found that blocking of ICAM-1 greatly decreased LNP uptake by Kupffer cells (Supplementary Fig. 16a–c). Moreover, sEVs from an *Icam-1* KO tumour cell line failed to improve LNP uptake (Supplementary Fig. 17a,b), further confirming the role of ICAM-1 in improving Kupffer cell uptake. Chemical conjugation of LNPs and sEVs further enhanced LNP delivery to Kupffer cells (Supplementary Fig. 17c,d). These results further demonstrated that the binding of sEVs to LNPs aids in the trafficking of LNPs to liver Kupffer cells. Next, we investigated the potential mechanism behind Kupffer cell uptake of LNPs. Since sEV uptake appeared to be mainly mediated by ICAM-1, we analysed the expression of Mac-1 subunits CD11b and CD18 in different primary liver cells, as Mac-1 can recognize ICAM-1 and initiate cell uptake. We found that liver Kupffer cells displayed the largest CD11b⁺CD18⁺ population compared with other liver cells (Fig. 2h, Supplementary Fig. 18a–f and Supplementary Figs. 19 and 20). This is consistent with a recent publication showing that tumour-derived sEVs can traffic to the liver and target liver Kupffer cells³⁷. Collectively, these results suggest that LNPs bind to sEVs and the resulting LNP–sEV complex can be delivered to liver Kupffer cells through the ICAM-1–Mac-1 interaction.

To further investigate the mechanism underlying LNP trafficking to Kupffer cells, we treated *Rab27a* KO tumour-bearing mice with DiR-labelled LNPs via intratumoural (i.t.) injection and analysed their biodistribution (Supplementary Fig. 21a). We found that only ~22% of LNPs trafficked to the liver. However, when injecting sEVs directly into the tumour, about 75% of the sEVs trafficked to the liver (Fig. 2i,j and Supplementary Fig. 21a). These results indicate that sEVs more

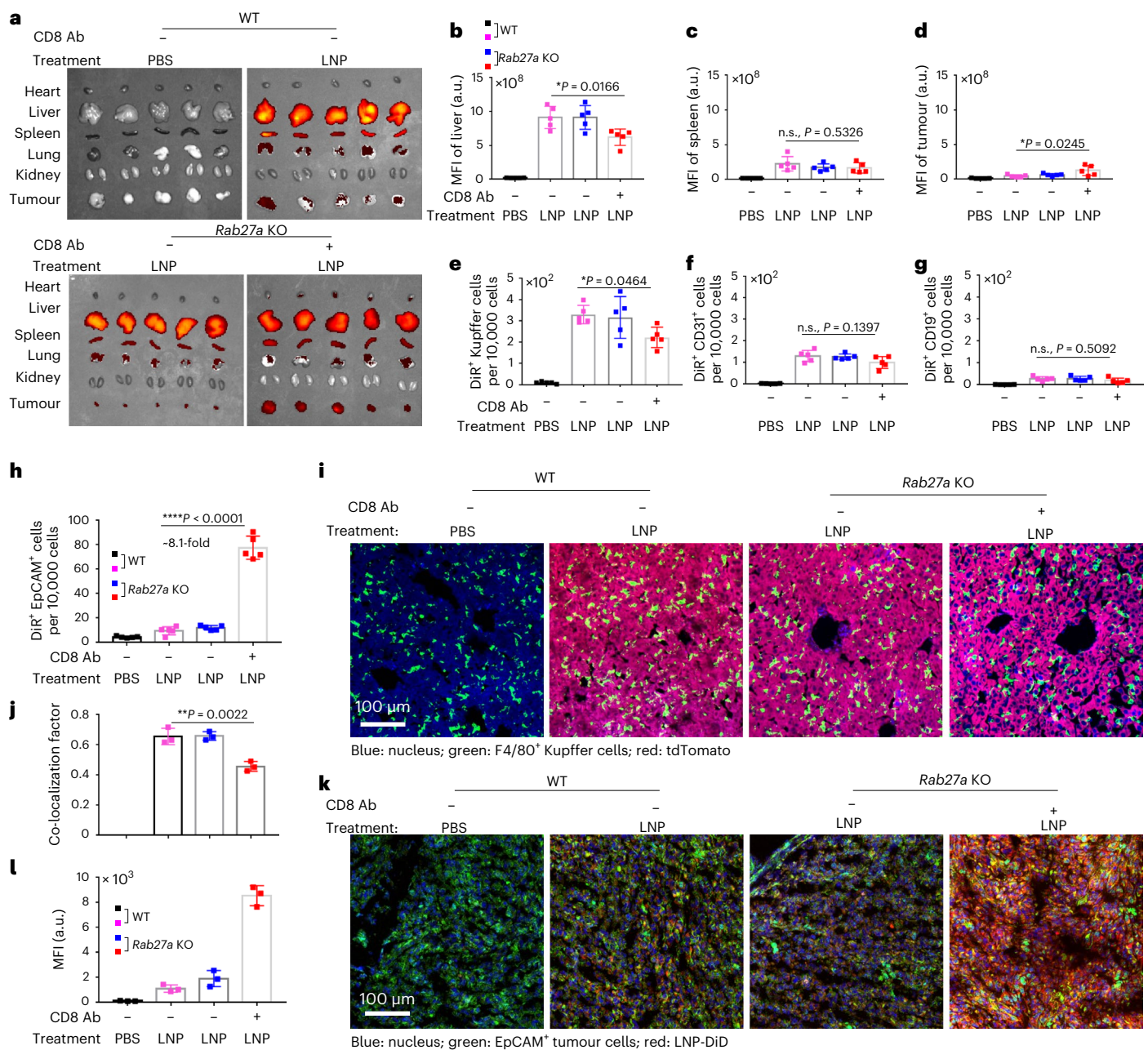


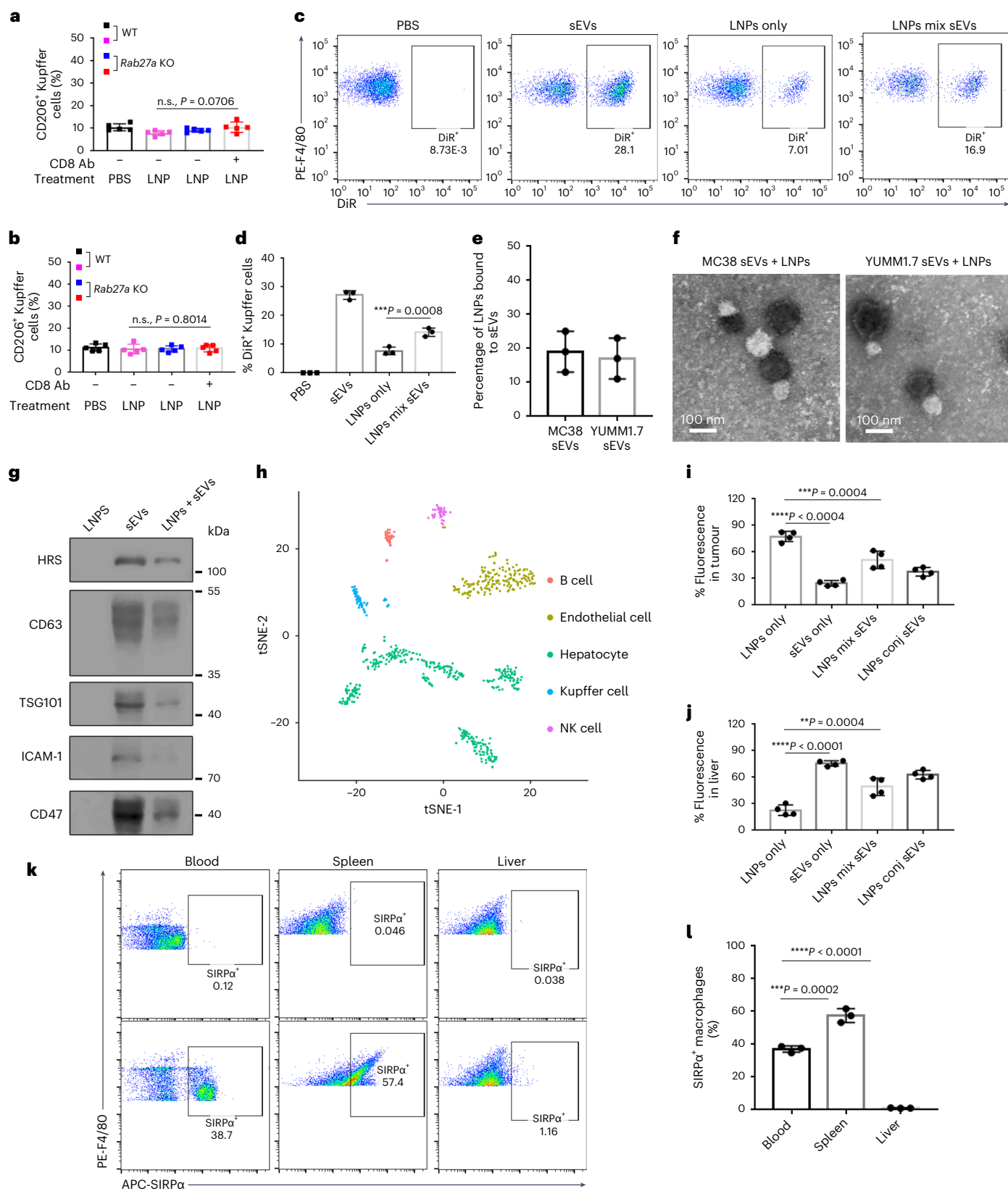
Fig. 1 *Rab27a* KO in tumour cells promotes the accumulation of LNPs in tumours. **a**, An anti-CD8 antibody was used to deplete CD8⁺ T cells in *Rab27a* KO MC38 tumour-bearing mice. LNP-DiR were i.v. injected, and after 24 h, mouse major organs and tumours were collected and imaged. **b–d**, Quantification of the mean fluorescence intensity (MFI) signal in the liver (**b**), spleen (**c**) and tumour (**d**). n.s., not significant. a.u., arbitrary units. **e–h**, DiR⁺ Kupffer cells (**e**), endothelial cells (**f**), B cells (**g**) and tumour cells (**h**) were quantified. **i**, Immunofluorescence images of Ail4 mouse livers and tumours showing the biodistribution of LNPs (Kupffer cells are shown in green and LNPs are shown in

red). **j**, Quantification of the overlap of the green (Kupffer cells) and red (LNPs) signal. **k**, Distribution of LNPs in tumour tissues (the nucleus is shown in blue, the tumour cells are shown in green and LNP-DiD is shown in red). **l**, Quantification of the overlap of green (tumour cells) signal and red (LNPs) signal. The data in **b–g**, **h**, **j** and **l** are shown as mean ± s.d. ($n = 5$ biological independent samples for **b–g** and $n = 3$ biological independent samples for **h**, **j** and **l**). One-way ANOVA with Tukey's post hoc test was used to analyse statistical differences unless specifically stated. * $P < 0.05$; ** $P < 0.01$; *** $P < 0.001$; **** $P < 0.0001$. The experiments were repeated three times with similar results.

heavily favour liver accumulation compared with LNPs. Moreover, pre-incubation of LNPs (labelled with DiR) with sEVs can increase the amount of LNPs that traffic to the liver (Fig. 2i,j and Supplementary Fig. 21a). In mice bearing WT tumours, the liver accumulation of LNPs was about 50% (Supplementary Fig. 21c). We speculate that this is a result of the formation of LNP-sEV complexes in the tumour tissue. Moreover, when chemically conjugating sEVs to LNPs, ~62% of LNPs trafficked to the liver (Fig. 2i,j and Supplementary Figs. 21a and 22). In contrast, when LNPs were injected subcutaneously (s.c.) into healthy

mice (without tumours), LNPs remained at the injection site and did not traffic to the liver (Supplementary Fig. 21b). These results provide further support for the connection between the physical interactions between LNPs and sEVs and their increase in trafficking from the tumour to the liver.

There are several variations of Mac1⁺ macrophages in different tissues³⁸. We, therefore, investigated why sEVs target liver macrophages but not other macrophages (Fig. 1e and Supplementary Figs. 3e and 4b). We found that the expression of SIRP α (recognition



of Mac1 by SIRP α mediates endocytosis inhibition) on liver Kupffer cells is much lower compared with macrophages in other tissues (Fig. 2k,l and Supplementary Fig. 23). The delivery of LNP–sEV complexes to Kupffer cells and not other types of macrophages may be partially attributable to this lower degree of SIRP α expression on Kupffer cells.

sEVs alter cellular uptake of LNPs in vitro

We next investigated the effect of sEVs on LNP delivery to tumour cells in vitro. We found that *Rab27a* KO greatly improved LNP cellular uptake (Fig. 3a), whereas sEV supplementation substantially decreased LNP uptake (Fig. 3b) in many tumour cell lines (Fig. 3c–f). High levels of SIRP α were detected in MC38, YUMM1.7, B16-F10 and WM9 tumour cell

Fig. 2 | Binding of LNP to sEVs promotes the delivery of LNPs to liver Kupffer cells. **a, b**, CD206 expression in liver Kupffer cells from MC38 (**a**) or YUMML7 (**b**) tumour-bearing mice. n.s., not significant. **c, d**, Liver cells were incubated with sEVs-DiR, LNP-DiR or sEVs pre-mixed with LNPs (where only LNPs were labelled with DiR). After 2 h, the DiR signal in Kupffer cells was analysed (**c**) and quantified (**d**). **e**, Percentage of LNPs bound to sEVs from MC38 cells or YUMML7 cells. **f**, TEM images showing LNPs bound to sEVs. **g**, Pulldown assay to assess LNP binding to sEVs. **h**, t-distributed stochastic neighbour embedding (tSNE) visualization plot of single-cell RNA sequencing data from healthy mouse liver cells. NK, natural killer. **i, j**, Different nanoparticles were i.t. injected to *Rab27a* KO

MC38 tumours: (1) LNP-DiR, (2) sEVs-DiR, (3) LNP-DiR mixed with sEVs and (4) LNP-DiR conjugated (conj.) to sEVs. After 24 h, mouse liver (**i**) and tumours (**j**) were imaged (Supplementary Fig. 21a) and quantified. **k**, Flow cytometry analysis of SIRP α expression in macrophages from blood, spleen or liver. **l**, Quantification of **k**. Data in **a, b, d, e, i, j** and **l** are shown as mean \pm s.d. ($n = 5$ biological independent samples for **a** and **b**, $n = 3$ biological independent samples for **d, e** and **l** and $n = 4$ biological independent samples for **i** and **j**). One-way ANOVA with Tukey's post hoc test was used to analyse statistical differences unless specifically mentioned. * $P < 0.05$; ** $P < 0.01$; *** $P < 0.001$; **** $P < 0.0001$. The experiments were repeated three times with similar results.

lines and many primary human tumour cells (Supplementary Fig. 24). sEVs binding to LNPs may, therefore, be responsible for decreased LNP uptake by tumour cells. Thus, we speculate that both sEV binding to LNPs and the CD47–SIRP α interaction decrease LNP uptake by tumour cells. In contrast to tumour cells, normal cells may not have such a defence system, as normal cells exhibited relatively low sEV secretion compared with tumour cells (Supplementary Fig. 25a). We also demonstrated that microvesicle (MV) inhibition did not affect LNP uptake (Supplementary Fig. 25b,c), probably due to the relatively low concentration of MVs compared with sEVs in culture medium (Supplementary Fig. 25b,c).

We further investigated the potential mechanisms underlying sEV-mediated LNP uptake inhibition. When treating tumour cells with an equivalent number of sEVs and LNPs, tumour cells take up more LNPs than sEVs (Supplementary Fig. 26a,b), likely because the CD47 molecules expressed on sEVs can be recognized by SIRP α expressed on tumour cells³⁹, inhibiting the uptake of sEVs. Moreover, we investigated if the added sEVs compete with LNPs for uptake or if they saturate the endocytic capacity of tumour cells. Our results showed that pretreatment with unlabelled LNP only slightly decreased the uptake of LNPs labelled with 3,3'-diiodoacetyl-5-(6-diethylamino)carboxyethyl carbocyanine perchlorate (DiO) (LNP-DiO) by MC38 cells, while pretreatment with unlabelled sEV greatly decreased LNP-DiO uptake (Supplementary Fig. 26c,d). Moreover, a blockade of the sEV surface marker CD47 greatly rescued sEV-mediated LNP uptake inhibition (Supplementary Fig. 26c,d). Altogether, these results demonstrate that sEV-dependent LNP uptake inhibition is mediated by CD47 on the sEV surface.

Considering that sEV binding to LNPs resulted in nanocomplexes with larger sizes, we investigated the effect of size increase on the uptake of the particles by MC38 cells (Supplementary Fig. 27a) and demonstrated that LNP size increase alone does not explain decreased uptake by tumour cells. We also investigated the effect of size increase on the uptake of LNPs by Kupffer cells and found that the uptake of larger LNPs (125 nm and 93 nm) by Kupffer cells is higher than that of more typically sized (66 nm) LNPs (Supplementary Fig. 27b). Moreover, we found that conjugation of LNP encapsulating Luc mRNA (LNP-mLuc) to sEVs greatly increased the uptake of LNP-mLuc by Kupffer cells, compared with conjugation of LNP-mLuc to LNP encapsulating eGFP mRNA (LNP-meGFP). However, blocking ICAM-1–Mac-1 interactions greatly decreased the uptake of LNP–sEV complexes (Supplementary Fig. 27c). These results demonstrate that both increased size and ICAM-1–Mac-1

interactions play important roles in increasing LNP uptake by Kupffer cells. Moreover, we found that even though sEVs derived from normal cells can also bind to LNPs, these sEVs only lead to moderate LNP uptake inhibition, probably due to their lower expression of SIRP α compared with sEVs derived from tumour cells (Supplementary Fig. 28a–d). Altogether, these results suggest that the sEV-mediated defence system is more restricted to tumour cells.

Next, we assessed if delivery of siRNA targeting *Rab27a* (*siRab27a*) can decrease sEV levels and, thus, improve nanoparticle delivery to tumour cells. *Rab27a* knockdown greatly decreased sEV secretion (Supplementary Fig. 29a–c) and increased enhanced green fluorescent protein (eGFP) expression (Fig. 3g) mediated by LNP-meGFP and luciferase expression (Fig. 3h) mediated by LNP-mLuc. Moreover, knockdown of *Rab27a* also enhanced the delivery of LNPs encapsulating mRNA encoding tensin homologue deleted on chromosome 10 (*Pten*)⁴⁰ (*mPten*) to YUMML7 cells (Supplementary Fig. 29d) and a mRNA encoding the stimulator of interferon genes (*mSting*) in MC38 cells (Supplementary Fig. 30a). These results demonstrate that knockdown of *Rab27a* to decrease sEV secretion can improve in vitro LNP transfection.

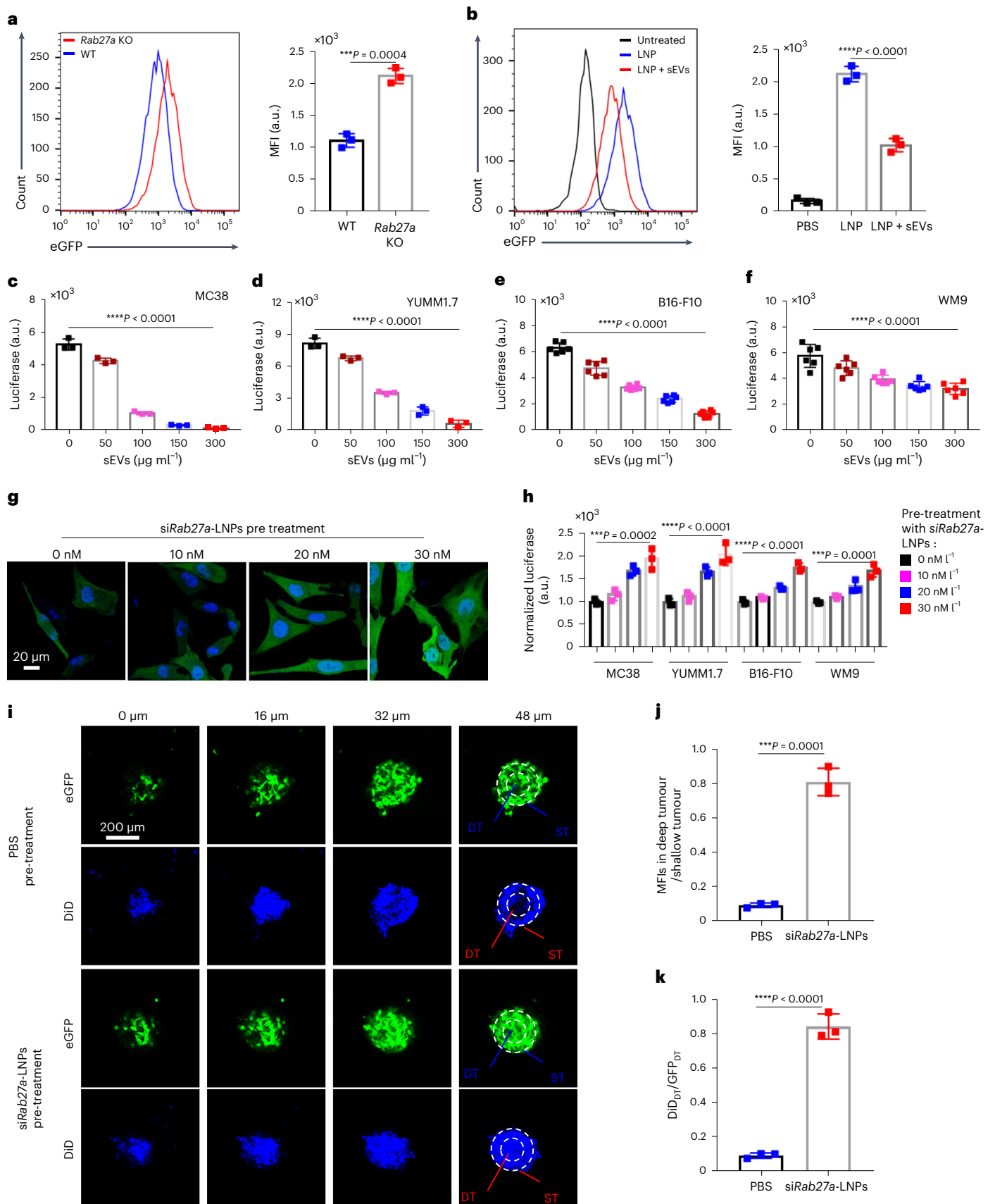
We then asked if *siRab27a* delivery can improve the penetration of LNPs in a tumour spheroid model⁴¹ (Fig. 3i–k). We found that *siRab27a*-LNP pretreatment substantially improved the spheroid penetration of 1,1'-diiodoacetyl-3,3,3'-tetramethylindodicarbocyanine (DiD)-labelled LNPs (Fig. 3i–k and Supplementary Fig. 31). We investigated if the improved LNP penetration is a result of the increase in nanoparticle size and found that, in *Rab27a* KO MC38 tumour spheroids, increasing the size of LNPs leads to slightly decreased LNP penetration. A similar trend was observed in WT MC38 tumour spheroids. However, the penetration of LNPs was substantially lower in WT MC38 tumour spheroids than in *Rab27a* KO MC38 spheroids, irrespective of LNP size (Supplementary Fig. 32). These results indicate that both the increase in particle size and the high sEV concentration facilitated the exclusion of the sEV–LNP complex from the tumour. Collectively, our results show that inhibition of sEV secretion improves tumour spheroid penetration.

Suppression of sEVs improves *Pten* mRNA delivery in vivo

Next, we investigated whether decreasing sEV levels in tumour tissue improves LNP accumulation in tumours. We first investigated if LNPs co-delivering *siRab27a* and a scrambled mRNA can knockdown the

Fig. 3 | sEVs act as a defence system against lipid nanoparticle-based mRNA delivery. **a**, eGFP expression was measured in WT or *Rab27a* KO MC38 cells following treatment with LNPs encapsulating eGFP mRNA (LNP-meGFP) for 24 h. **b**, eGFP expression was measured in *Rab27a* KO cells treated with LNP-meGFP for 24 h in the presence or absence of sEVs. **c–f**, MC38 (**c**), YUMML7 (**d**), B16-F10 (**e**) and WM9 (**f**) cells were treated with LNPs encapsulating luciferase mRNA (LNP-mLuc) in the presence of sEVs for 24 h, and the luciferase expression was measured. **g**, WT MC38 cells were incubated with LNPs encapsulating *siRab27a* (LNP-*siRab27a*) for 24 h and then treated with fresh medium containing LNP-meGFP for 24 h before eGFP expression was measured. **h**, Cells were treated with LNP-*siRab27a* for 24 h and then with fresh media containing LNP-mLuc for 24 h, after which luciferase expression in the cells was analysed. **i–k**, tumour spheroids were pretreated with PBS or LNP-*siRab27a* for 24 h and then the

tumour spheroids were treated with fresh media containing DiD-labelled LNPs for another 24 h before the penetration of DiD-labelled LNPs was characterized (**i**). The ratio of DiD signals in deep tumour spheroids to that in shallow tumour spheroids is quantified in **j**. The ratio of DiD signal in deep tumour (DiD_{DT}) spheroids to eGFP signal in deep tumour (GFP_{DT}) spheroids after PBS or LNP-*siRab27a* treatment is quantified in **k**. The data are shown as mean \pm s.d. ($n = 3$ biological independent samples for **a** (right), **b** (right) and **c, d, h, j** and **k**; $n = 6$ biological independent samples for **e** and **f**). Statistical analysis in **b–f** and **h** was performed using one-way ANOVA with Tukey's post hoc test. For statistical analysis in **a, j** and **k**, a two tailed unpaired Student's *t*-test was used. * $P < 0.05$; ** $P < 0.01$; *** $P < 0.001$; **** $P < 0.0001$. The experiments were repeated three times with similar results. MFI, mean fluorescence intensity; a.u., arbitrary unit; GFP, green fluorescent protein.



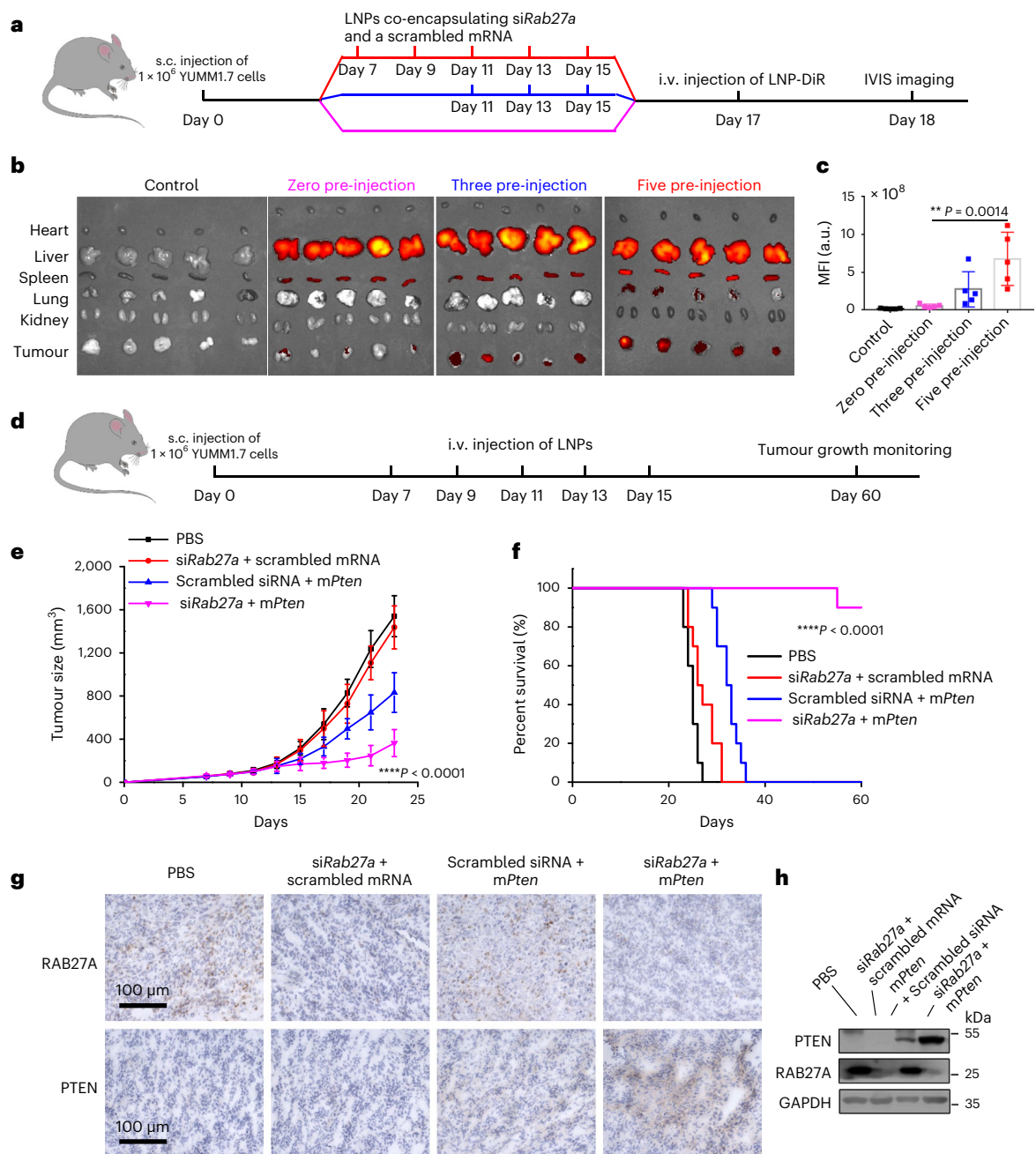


Fig. 4 | Rab27a knockdown enhances LNP tumour delivery and the anti-tumour efficacy of *Pten* mRNA. **a, b**, YUMM1.7 tumour-bearing mice were treated with zero, three or five injections of LNP co-encapsulating *siRab27a* and scrambled mRNA. A total of 48 h after the last injection (day 17), LNP-DiR was i.v. injected (**a**). Biodistribution of LNP-DiR in major organs and tumours was determined (**b**). **c**, Quantification of DiR signal in tumour tissues. **d**, Tumour-bearing mice were i.v. injected with LNPs encapsulating indicated RNAs at days 7, 9, 11, 13 and 15. **e, f**, Tumour growth curves (**e**) and survival curves (**f**), respectively.

g, h, Immunohistochemistry (**g**) and western blot analysis (**h**) of RAB27A and PTEN expression in tumours collected on day 23. The data in **c**, **e** and **f** are shown as mean \pm s.d. ($n = 5$ biological independent samples for **c**; $n = 10$ biological independent samples for **e** and **f**). The statistical differences in **c** and **e** were calculated using one-way ANOVA with Tukey's post hoc test. The statistical differences in **f** were calculated using a Mantel-Cox two-sided log-rank test. * $P < 0.05$; ** $P < 0.01$; *** $P < 0.001$; **** $P < 0.0001$. The experiments were repeated three times with similar results.

Rab27a gene and decrease sEVs in tumour tissue (Fig. 4a). While mice with no pre-injections of *siRab27a*-loaded LNP showed very low LNP-DiR signal at the tumour site, those with three and five pre-injections of *siRab27a*-loaded LNP showed substantially decreased *Rab27a* expression and sEV secretion in the tumour tissue (Fig. 4b and Supplementary Fig. 33). These eventually increased LNP-DiR signal in the tumour (Fig. 4c).

We investigated if co-delivery of *siRab27a* and *mPten* could elicit an anti-tumour effect. YUMM1.7 tumour-bearing mice were treated with: (1) LNPs co-encapsulating *siRab27a* and scrambled mRNA,

(2) LNPs co-encapsulating scrambled siRNA and *mPten* or (3) LNPs co-encapsulating *siRab27a* and *mPten* (Fig. 4d). All mice were imaged at day 23 (Supplementary Fig. 33g). LNPs co-encapsulating *siRab27a* and *mPten* led to the greatest tumour growth inhibition and the longest mouse survival compared with other treatments without inducing body weight loss (Fig. 4e, f and Supplementary Fig. 33g, h). We repeated this animal experiment and found that *Rab27a* expression was greatly decreased in tumour tissues collected from mice treated with LNPs co-encapsulating *siRab27a* and *mPten* (Fig. 4g, h). Moreover, LNP treatment also increased PTEN and cleaved caspase-3 expression

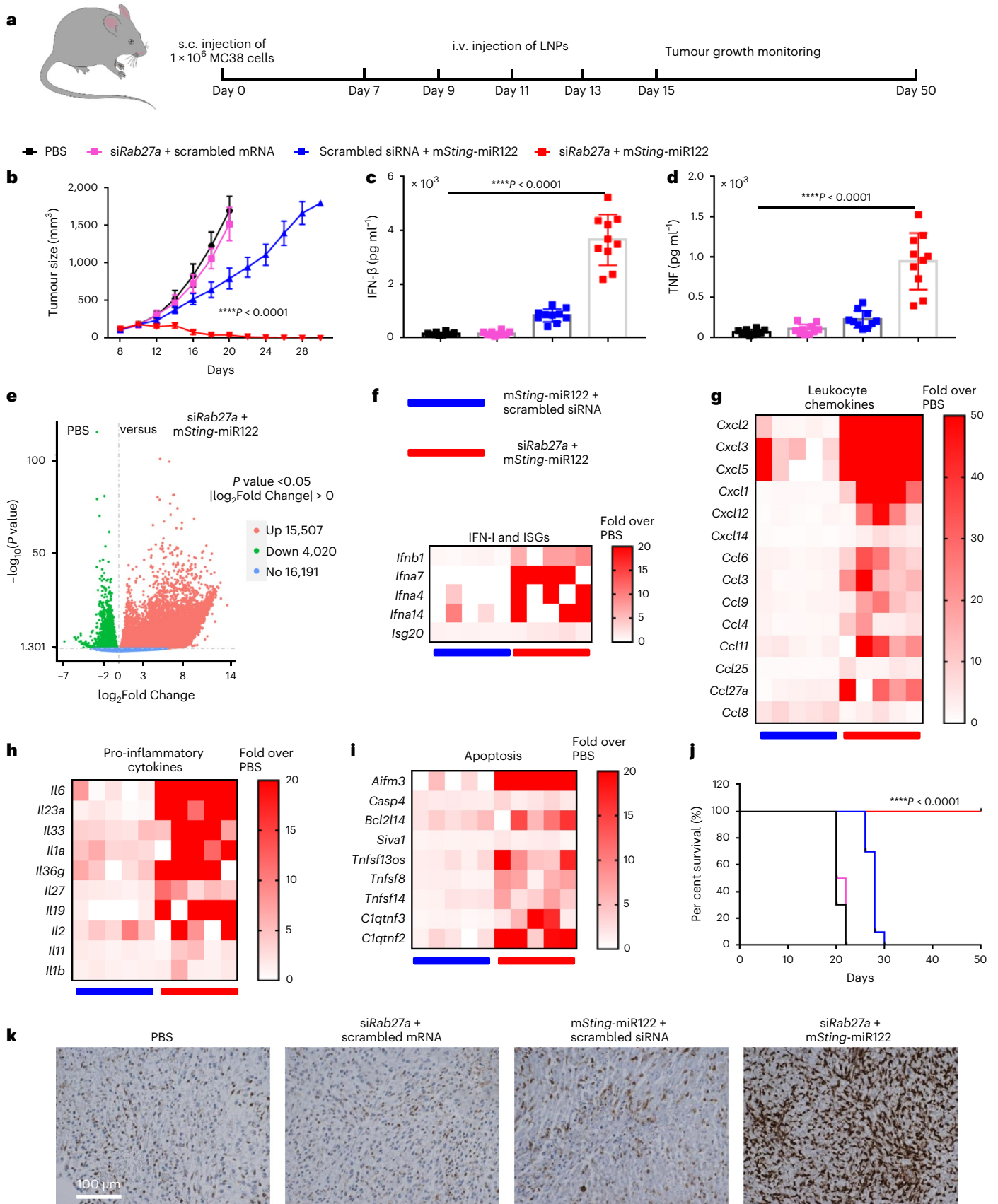


Fig. 5 | *Rab27a* knockdown enhances the anti-tumour efficacy of a *Sting* mRNA. **a**, MC38 tumour-bearing mice were i.v. injected with LNP co-encapsulating *siRab27a* and scrambled mRNA, LNP co-encapsulating scrambled *siRNA* and *mSting*-miR-122 or LNP co-encapsulating *siRab27a* and *mSting*-miR-122 at days 7, 9, 11, 13 and 15. **b**, Tumour growth curves. **c,d**, Quantification of IFN- β (**c**) and TNF (**d**) concentrations in tumour tissues. **e**, RNA sequencing data from tumour tissues. Volcano plots of differentially expressed genes due to treatment with LNP co-encapsulating *siRab27a* and *mSting*-miR-122 compared with PBS treatment. **f–i**, Heat map of selected differential expressed genes (DEGs) including type-I interferon (IFN-I) and interferon-stimulated genes (ISGs) (**f**),

leukocyte chemokines (**g**), pro-inflammatory cytokines (**h**) and apoptosis genes (**i**) in response to treatment with LNP co-encapsulating scrambled *siRNA* and *mSting*-miR-122 or LNP co-encapsulating *siRab27a* and *mSting*-miR-122. **j**, Mouse survival curves. **k**, Immunohistochemistry images showing the expression of STING in tumour tissues. The data in **b**, **c**, **d** and **j** are presented as mean \pm s.d. ($n = 10$ biological independent samples). The statistical differences in **b**, **c** and **d** were calculated using one-way ANOVA with Tukey's post hoc test for multiple comparisons. The statistical difference in **j** was calculated using a Mantel–Cox two-sided log-rank test. * $P < 0.05$; ** $P < 0.01$; *** $P < 0.001$; **** $P < 0.0001$. The experiments were repeated three times with similar results.

while decreasing Ki67 and Bcl-2 expression (Fig. 4g and Supplementary Fig. 34a). Importantly, we found that this treatment induced negligible toxicity to major organs (Supplementary Fig. 34b), indicating the safety of this co-delivery strategy. After demonstrating that co-delivery of *siRab27a* and *mPten* can improve the therapeutic efficacy of *mPten*, we next evaluated if this co-delivery strategy could be applied for the improvement of other mRNA-based therapeutics.

Suppression of sEVs improve *Sting* mRNA delivery in vivo

STING has attracted increasing attention for immunotherapy in recent years⁴². Most current studies focus on the development of STING agonists to activate STING in tumours to induce anti-tumour immune responses⁴³. However, STING agonist-based tumour therapy is restricted due to the ease of degradation and low cell membrane permeability⁴⁴; moreover, many tumours do not express STING⁴⁵, further limiting the efficacy of STING agonists⁴⁶. Here we assess the potential of LNPs co-encapsulating *siRab27a* and a mRNA encoding a constitutively activated *Sting* (R283S) (*mSting*) for tumour therapy. We found that the successful delivery of *mSting* to cells can effectively activate downstream signaling (Supplementary Fig. 30b–l). However, treatment of mice with *mSting*-loaded LNPs led to rapid loss of body weight, elevated cytokine levels in the blood and liver damage (Supplementary Fig. 35), indicating toxicity, which we attributed to off-target translation of the STING cargo.

To solve the off-target issue, we added a microRNA-122 (miR-122) binding site in the 3' UTR of the *Sting* mRNA (*mSting*-miR-122) following a reported method⁴⁷ and found that hepatocyte cell toxicity was greatly decreased while tumour cell toxicity was maintained (Supplementary Fig. 36a,b). We then investigated the anti-tumour efficacy of *mSting*-miR-122-encapsulating LNPs in vivo. MC38 tumour-bearing mice were treated with LNPs encapsulating indicated RNAs (Fig. 5a). All mice were imaged on day 20 and their body weights were monitored during the treatment (Supplementary Fig. 37a,b). LNPs co-encapsulating *siRab27a* and *mSting*-miR-122 showed the greatest tumour growth suppression (Fig. 5b) compared with other treatments. Moreover, co-delivery of *siRab27a* and *mSting*-miR-122 enhanced the expression of interferon-beta (IFN- β) and tumor necrosis factor (TNF) in tumour tissue (Fig. 5c,d). RNA sequencing (Fig. 5e–i) data showed that the LNPs co-encapsulating *siRab27a* and *mSting*-miR-122 greatly

increased STING-downstream signaling (Fig. 5f–i) and extended mouse survival (Fig. 5j and Supplementary Fig. 37c–f). We repeated the animal experiment and found that LNPs co-encapsulating *siRab27a* and *mSting*-miR-122 greatly increased STING and cleaved caspase-3 expression while decreasing Ki67 and Bcl-2 expression in tumour tissue (Fig. 5k and Supplementary Fig. 37g).

Compared with treatment with *siRab27a* and unmodified *mSting*, limited toxicity was induced in mice treated with LNP co-encapsulating *siRab27a* and *mSting*-miR-122. Blood biochemistry analysis and haematoxylin and eosin (H&E) staining assay demonstrated that the levels of liver enzymes and various blood cytokines were maintained in normal ranges, and *mSting*-miR-122 did not induce major organ damage (Extended Data Fig. 1a–f).

sEVs act as a defence system against other therapeutics

Finally, we examined if the sEV-based defence system is applicable to other nanoparticle-based delivery systems and tumour therapy modalities. Organic nanoparticles, such as liposomes, polylactic-co-glycolic acid (PLGA) nanoparticles, polystyrene (PS) nanoparticles and inorganic nanoparticles such as gold nanoparticles and silica nanoparticles, were characterized (Supplementary Table 1). The internalization of various nanoparticles by *Rab27a* KO cells was found to be higher than that of WT cells. Moreover, when adding sEVs to culture medium, the uptake of different nanoparticles by *Rab27a* KO cells decreased in a sEV dose-dependent manner (Fig. 6a–h and Supplementary Fig. 38a–d), as these particles can also bind to tumour cell sEVs (Supplementary Fig. 38e–h). These results demonstrate that tumour cell sEVs act as a defence system against various nanoparticles.

Since oncolytic virus therapy and antibody therapies have shown great success in the clinic⁴⁸, we examined whether tumour sEVs also affect these therapeutics. A lentiviral construct that delivers a luciferase reporter was used as a model virus to infect cells. The expression of luciferase by *Rab27a* KO cells was much higher than that of the WT cells (Fig. 6g). Moreover, when adding sEVs to the culture medium, an sEV dose-dependent decrease in luciferase expression was observed (Fig. 6h). Similarly, we demonstrated that many therapeutic antibodies^{49,50} that need to bind to the tumour cell surface to exert their functions can also be affected by tumour cell sEVs, including anti-epidermal growth factor receptor (EGFR) antibody and anti-programmed death

Fig. 6 | Tumour cell-derived extracellular vesicles act as a defence system against other nanoparticles and tumour therapeutics. **a–f**, Effect of sEVs on the cellular uptake of nanoparticles including liposomes (**a** and **b**), PLGA nanoparticles (**c** and **d**) and PS nanoparticles (**e** and **f**). Dye-labelled nanoparticles were incubated with WT or *Rab27a* KO MC38 cells for 24 h. Nanoparticle accumulation was determined by measuring the mean fluorescence intensity of cells using flow cytometry (**a**, **c** and **e**). *Rab27a* KO cells were treated with liposomes (**b**), PLGA nanoparticles (**d**) and PS nanoparticles (**f**) in the presence of increasing amounts of sEVs for 24 h before analysis of fluorescence intensity. **g**, Luciferase expression levels of WT or *Rab27a* KO cells treated with a lentivirus delivering a luciferase reporter gene. **h**, Luciferase expression levels of *Rab27a* KO MC38 cells treated with lentivirus in the presence of increasing amounts of sEVs. **i–l**, The effect of sEVs on the binding of anti-EGFR antibody (**i** and **j**) and

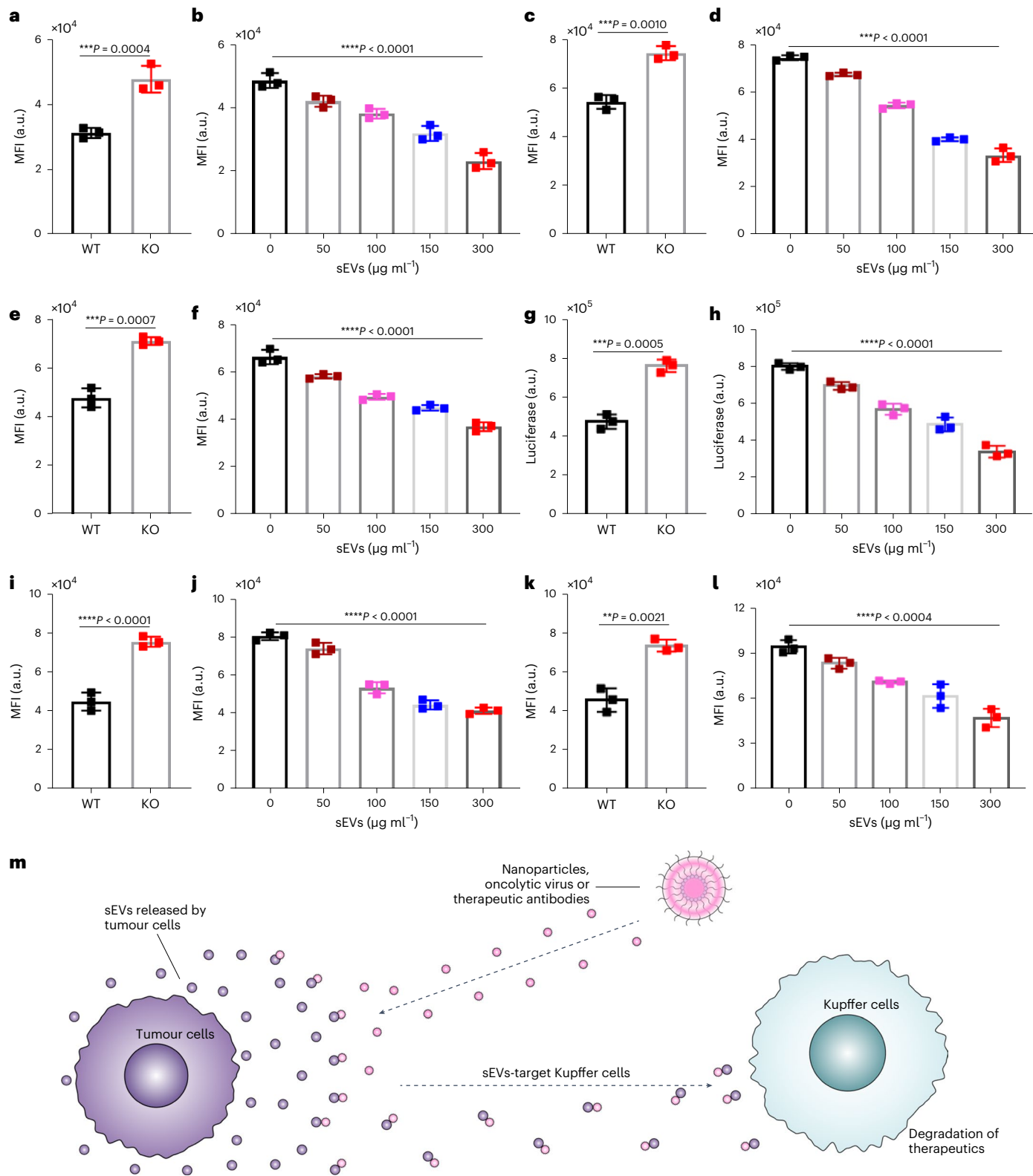
anti-PD-L1 antibody (**k** and **l**) to tumour cells. WT or *Rab27a* KO MC38 cells were treated with anti-EGFR antibody (**i**) or anti-PD-L1 antibody (**k**) for 30 min before determining antibody binding by flow cytometry. *Rab27a* KO cells were treated with anti-EGFR antibody (**j**) or anti-PD-L1 antibody (**l**) in the presence of different amounts of sEVs for 30 min. Then, binding of the antibody to cells was measured using flow cytometry. **m**, Schematic illustration of the mechanism of the tumour cell sEV-mediated defence system. The data in **a–l** are shown as mean \pm s.d. ($n = 3$ biological independent samples). The statistical differences in **a**, **c**, **e**, **g**, **i** and **k** were calculated using a two-tailed unpaired Student's *t*-test. The statistical differences in **b**, **d**, **f**, **h**, **j** and **l** were calculated using one-way ANOVA with Tukey's post hoc test. * $P < 0.05$; ** $P < 0.01$; *** $P < 0.001$; **** $P < 0.0001$. The experiments were repeated three times with similar results. MFI, mean fluorescence intensity; a.u., arbitrary unit.

ligand 1 (PD-L1) antibody (Fig. 6i–l). These results demonstrate that the sEV-based defence system is also applicable to viral- and antibody-based tumour therapeutics.

Outlook

The findings made in this study may influence other nanoparticle-based therapies in the clinic¹. For example, Doxil, a doxorubicin liposome, has been shown to accumulate in Kupffer cells⁵¹. Overcoming the sEV

defence system in tumours may improve the anti-tumour efficacy of Doxil. Future studies will explore the sEV-based defence system in other tumour types, such as breast, pancreatic, lung, prostate and liver tumours. We will also explore how sEVs interact with other particles while maintaining their own stability. The development of strategies that can effectively overcome the sEV-based defence system to improve disease treatment will also be a direction that we will pursue in the future.



Online content

Any methods, additional references, Nature Portfolio reporting summaries, source data, extended data, supplementary information, acknowledgements, peer review information; details of author contributions and competing interests; and statements of data and code availability are available at <https://doi.org/10.1038/s41563-024-01961-6>.

References

1. D'Mello, S. R. et al. The evolving landscape of drug products containing nanomaterials in the United States. *Nat. Nanotech.* **12**, 523–529 (2017).
2. van der Meel, R. et al. Smart cancer nanomedicine. *Nat. Nanotech.* **14**, 1007–1017 (2019).
3. Sindhvani, S. et al. The entry of nanoparticles into solid tumours. *Nat. Mater.* **19**, 566–575 (2020).
4. Wilhelm, S. et al. Analysis of nanoparticle delivery to tumours. *Nat. Rev. Mater.* **1**, 1–12 (2016).
5. Sykes, E. A., Chen, J., Zheng, G. & Chan, W. C. Investigating the impact of nanoparticle size on active and passive tumor targeting efficiency. *ACS Nano* **8**, 5696–5706 (2014).
6. Zhang, Y. R. et al. Strategies to improve tumor penetration of nanomedicines through nanoparticle design. *Wires Nanomed. Nanobi.* **11**, e1519 (2019).
7. Choi, K. Y. et al. Self-assembled hyaluronic acid nanoparticles for active tumor targeting. *Biomaterials* **31**, 106–114 (2010).
8. Kong, S. M., Costa, D. F., Jagielska, A., Van Vliet, K. J. & Hammond, P. T. Stiffness of targeted layer-by-layer nanoparticles impacts elimination half-life, tumor accumulation, and tumor penetration. *Proc. Natl Acad. Sci. USA* **118**, e2104826118 (2021).
9. Acharya, S. & Sahoo, S. K. PLGA nanoparticles containing various anticancer agents and tumour delivery by EPR effect. *Adv. Drug Del. Rev.* **63**, 170–183 (2011).
10. Bazak, R., Hour, M., El Achy, S., Kamel, S. & Refaat, T. Cancer active targeting by nanoparticles: a comprehensive review of literature. *J. Cancer Res. Clin. Oncol.* **141**, 769–784 (2015).
11. Cedervall, T. et al. Understanding the nanoparticle–protein corona using methods to quantify exchange rates and affinities of proteins for nanoparticles. *Proc. Natl Acad. Sci. USA* **104**, 2050–2055 (2007).
12. Zhang, T. et al. Magnetothermal regulation of in vivo protein corona formation on magnetic nanoparticles for improved cancer nanotherapy. *Biomaterials* **276**, 121021 (2021).
13. Zhang, Y.-N., Poon, W., Tavares, A. J., McGilvray, I. D. & Chan, W. C. Nanoparticle–liver interactions: cellular uptake and hepatobiliary elimination. *J. Control. Release* **240**, 332–348 (2016).
14. Nia, H. T., Munn, L. L. & Jain, R. K. Physical traits of cancer. *Science* **370**, eaaz0868 (2020).
15. Stylianopoulos, T. et al. Causes, consequences, and remedies for growth-induced solid stress in murine and human tumors. *Proc. Natl Acad. Sci. USA* **109**, 15101–15108 (2012).
16. Chen, Y. et al. Vasodilator hydralazine promotes nanoparticle penetration in advanced desmoplastic tumors. *ACS Nano* **13**, 1751–1763 (2019).
17. Fukumura, D. & Jain, R. K. Tumor microvasculature and microenvironment: targets for anti-angiogenesis and normalization. *Microvasc. Res.* **74**, 72–84 (2007).
18. Binnewies, M. et al. Understanding the tumor immune microenvironment (TIME) for effective therapy. *Nat. Med.* **24**, 541–550 (2018).
19. Dai, Y., Xu, C., Sun, X. & Chen, X. Nanoparticle design strategies for enhanced anticancer therapy by exploiting the tumour microenvironment. *Chem. Soc. Rev.* **46**, 3830–3852 (2017).
20. Gong, F. et al. Tumor microenvironment-responsive intelligent nanoplatforms for cancer theranostics. *Nano Today* **32**, 100851 (2020).
21. Zieren, R. C. et al. Extracellular vesicle isolation from human renal cancer tissue. *Med. Oncol.* **37**, 1–11 (2020).
22. Silva, J. et al. Analysis of exosome release and its prognostic value in human colorectal cancer. *Genes Chromosomes Cancer* **51**, 409–418 (2012).
23. Miller, I. V. & Grunewald, T. G. Tumour-derived exosomes: tiny envelopes for big stories. *Biol. Cell* **107**, 287–305 (2015).
24. Ostrowski, M. et al. Rab27a and Rab27b control different steps of the exosome secretion pathway. *Nat. Cell Biol.* **12**, 19–30 (2010).
25. Poggio, M. et al. Suppression of exosomal PD-L1 induces systemic anti-tumor immunity and memory. *Cell* **177**, 414–427. e413 (2019).
26. Chen, G. et al. Exosomal PD-L1 contributes to immunosuppression and is associated with anti-PD-1 response. *Nature* **560**, 382–386 (2018).
27. Fan, Y. et al. Exosomal PD-L1 retains immunosuppressive activity and is associated with gastric cancer prognosis. *Ann. Surg. Oncol.* **26**, 3745–3755 (2019).
28. Kim, D. H. et al. Exosomal PD-L1 promotes tumor growth through immune escape in non-small cell lung cancer. *Exp. Mol. Med.* **51**, 1–13 (2019).
29. Monypenny, J. et al. ALIX regulates tumor-mediated immunosuppression by controlling EGFR activity and PD-L1 presentation. *Cell Rep.* **24**, 630–641 (2018).
30. Ricklefs, F. L. et al. Immune evasion mediated by PD-L1 on glioblastoma-derived extracellular vesicles. *Sci. Adv.* **4**, eaar2766 (2018).
31. Yang, Y. et al. Exosomal PD-L1 harbors active defense function to suppress T cell killing of breast cancer cells and promote tumor growth. *Cell Res.* **28**, 862–864 (2018).
32. Gargiulo, E. et al. Extracellular vesicle secretion by leukemia cells in vivo promotes CLL progression by hampering antitumor T-cell responses. *Blood Cancer Discov.* **4**, 54–77 (2022).
33. Billingsley, M. M. et al. Ionizable lipid nanoparticle-mediated mRNA delivery for human CAR T cell engineering. *Nano Lett.* **20**, 1578–1589 (2020).
34. Ruiz-Alcaraz, A. J. et al. Characterization of human peritoneal monocyte/macrophage subsets in homeostasis: phenotype, GATA6, phagocytic/oxidative activities and cytokines expression. *Sci. Rep.* **8**, 1–14 (2018).
35. Jing, H., Sinha, S., Sachar, H. S. & Das, S. Interactions of gold and silica nanoparticles with plasma membranes get distinguished by the van der Waals forces: implications for drug delivery, imaging, and theranostics. *Colloids Surf., B* **177**, 433–439 (2019).
36. Tian, T. et al. Exosome uptake through clathrin-mediated endocytosis and macropinocytosis and mediating miR-21 delivery. *J. Biol. Chem.* **289**, 22258–22267 (2014).
37. Wang, G. et al. Tumour extracellular vesicles and particles induce liver metabolic dysfunction. *Nature* **618**, 374–382 (2023).
38. Springer, T., Galfré, G., Secher, D. S. & Milstein, C. Mac-1: a macrophage differentiation antigen identified by monoclonal antibody. *Eur. J. Immunol.* **9**, 301–306 (1979).
39. Kamekar, S. et al. Exosomes facilitate therapeutic targeting of oncogenic KRAS in pancreatic cancer. *Nature* **546**, 498–503 (2017).
40. Simpson, L. & Parsons, R. PTEN: life as a tumor suppressor. *Exp. Cell. Res.* **264**, 29–41 (2001).
41. Huang, K. et al. Size-dependent localization and penetration of ultrasmall gold nanoparticles in cancer cells, multicellular spheroids, and tumors in vivo. *ACS Nano* **6**, 4483–4493 (2012).
42. Barber, G. N. STING: infection, inflammation and cancer. *Nat. Rev. Immunol.* **15**, 760–770 (2015).
43. Le Naour, J., Zitvogel, L., Galluzzi, L., Vacchelli, E. & Kroemer, G. Trial watch: STING agonists in cancer therapy. *Oncoimmunology* **9**, 1777624 (2020).

44. Dane, E. L. et al. STING agonist delivery by tumour-penetrating PEG-lipid nanodiscs primes robust anticancer immunity. *Nat. Mater.* **21**, 710–720 (2022).
45. De Queiroz, N. M. G. P., Xia, T., Konno, H. & Barber, G. N. Ovarian cancer cells commonly exhibit defective STING signaling which affects sensitivity to viral OncolysisSTING signaling in ovarian cancer. *Mol. Cancer Res.* **17**, 974–986 (2019).
46. Liu, W. et al. Selective reactivation of STING signaling to target Merkel cell carcinoma. *Proc. Natl Acad. Sci. USA* **117**, 13730–13739 (2020).
47. Jain, R. et al. MicroRNAs enable mRNA therapeutics to selectively program cancer cells to self-destruct. *Nucleic Acid Ther.* **28**, 285–296 (2018).
48. Kaufman, H. L. & Maciorowski, D. Advancing oncolytic virus therapy by understanding the biology. *Nat. Rev. Clin. Oncol.* **18**, 197–198 (2021).
49. Heinemann, V., Stintzing, S., Kirchner, T., Boeck, S. & Jung, A. Clinical relevance of EGFR-and KRAS-status in colorectal cancer patients treated with monoclonal antibodies directed against the EGFR. *Cancer Treat. Rev.* **35**, 262–271 (2009).
50. Kimiz-Gebologlu, I., Gulce-Iz, S. & Biray-Avci, C. Monoclonal antibodies in cancer immunotherapy. *Mol. Biol. Rep.* **45**, 2935–2940 (2018).
51. Ohara, Y. et al. Effective delivery of chemotherapeutic nanoparticles by depleting host Kupffer cells. *Int. J. Cancer* **131**, 2402–2410 (2012).

Publisher's note Springer Nature remains neutral with regard to jurisdictional claims in published maps and institutional affiliations.

Springer Nature or its licensor (e.g. a society or other partner) holds exclusive rights to this article under a publishing agreement with the author(s) or other rightsholder(s); author self-archiving of the accepted manuscript version of this article is solely governed by the terms of such publishing agreement and applicable law.

© The Author(s), under exclusive licence to Springer Nature Limited 2024

¹Department of Bioengineering, University of Pennsylvania, Philadelphia, PA, USA. ²Division of Life Sciences and Medicine, Center for BioAnalytical Chemistry, Hefei National Research Center for Physical Science at the Microscale, University of Science and Technology of China, Hefei, China. ³Department of Biology, School of Arts and Sciences, University of Pennsylvania, Philadelphia, PA, USA. ⁴Department of Medicine, University of Pennsylvania, Philadelphia, PA, USA. ⁵Department of Biomedical Sciences, School of Veterinary Medicine, University of Pennsylvania, Philadelphia, PA, USA. ⁶Department of Chemistry, Tsinghua University, Beijing, China. ⁷Chinese Academy of Sciences Center for Excellence in Nanoscience, National Center for Nanoscience and Technology, Beijing, China. ⁸Penn institute for RNA innovation, University of Pennsylvania, Philadelphia, PA, USA. ⁹Abramson Cancer Center, Perelman School of Medicine, University of Pennsylvania, Philadelphia, PA, USA. ¹⁰Institute for Immunology, Perelman School of Medicine, University of Pennsylvania, Philadelphia, PA, USA. ¹¹Cardiovascular Institute, Perelman School of Medicine, University of Pennsylvania, Philadelphia, PA, USA. ¹²Institute for Regenerative Medicine, Perelman School of Medicine, University of Pennsylvania, Philadelphia, PA, USA. ¹³These authors contributed equally: Ningqiang Gong, Wenqun Zhong, Mohamad-Gabriel Alameh. ✉e-mail: dreww@upenn.edu; guowei@sas.upenn.edu; mjmitch@seas.upenn.edu

Methods

Chemicals and antibodies

DLin-MC3-DMA was purchased from MedChem Express. DiR was bought from Invitrogen. 1,2-distearoyl-*sn*-glycero-3-phosphocholine, cholesterol and 1,2-dimyristoyl-*rac*-glycero-3-methoxypolyethylene glycol-2000 (DMG-PEG 2000) were purchased from Avanti Polar Lipids. Anti-mouse F4/80 (clone: BM8, cat. no. 123110, 1:100 dilution), anti-mouse CD19 (clone: 6D5, cat. no. 115538, 1:100 dilution), anti-mouse CD3 (clone: OKT3, cat. no. 317306, 1:100 dilution), anti-mouse CD31 (clone: 390, cat. no. 102410, 1:100 dilution), anti-mouse CD11c (clone: N418, cat. no. 117310, 1:100 dilution), anti-mouse PD-L1 (clone: 10F.9G2, cat. no. 124312, 1:100 dilution) and anti-mouse EGFR (clone: H11, cat. no. MA5-13070, 1:100 dilution) were purchased from Thermo Fisher. Anti-mouse EpCAM (clone: VU-1D9, cat. no. NBP2-33078PECY55, 1:100 dilution) was obtained from NOVUS Biologicals. Anti-mouse TRP1 antibody (clone: EPR13063, cat. no. ab178676, 1:100 dilution) was ordered from Abcam. The Live/Dead Fixable Aqua Dead Cell Stain Kit was obtained from Thermo Fisher (cat. no. L34957). PLentipuro3/TO/V5-GW/EGFP-Firefly luciferase plasmid was purchased from Addgene (plasmid #119816). PS nanoparticles with COOH groups on the surface were purchased from Phosphorex (cat. no. 103).

Cell lines and animals

The human melanoma cell lines WM9 were established in Meenhard Herlyn's laboratory (The Wistar Institute) (cat. no. WM9-01-0001). The murine colon cancer cell line MC38 was purchased from Sigma-Aldrich (cat. no. SCC172). Other cell lines including YUMM1.7 (cat. no. CRL-3362), B16-F10 (cat. no. CRL-6475), NIH3T3 (cat. no. CRL-1658) and 293T (cat. no. CRL-3216) were obtained from ATCC. All cell lines tested negative for mycoplasma at the University of Pennsylvania Cell Center. The 200 C57BL/6J mice (female, 6–8 weeks) were ordered from Jackson laboratory (strain #000664) and housed in a specific-pathogen-free animal facility. Ai14 mice (female, 6–8 weeks) were from Jackson laboratory (strain #:007914). All protocols performed on animals in this article were approved by the institutional animal care and use committee of the University of Pennsylvania (protocol number 806540). The maximal tumour size/burden permitted by the ethics committee is 2 cm. We confirmed that during this study, the size limit was not reached.

Construction of *Rab27a* and *Icam-1*-KO cell lines

The guide RNA targeting murine *Rab27a* (sgRNA 1, 5'-CCAAGGCCAAGAAGCTTGATG-3', sgRNA 2, 5'-CATCAAGTCTTGGCCTTGG-3') (synthesized by Genewiz) and murine *Icam-1* (sgRNA 1, 5'-GAAGGCTTCTCTGGGATGGA-3', sgRNA 2, 5'-GCAGGAAGGCTTCTCTGGA-3') were annealed and cloned into lentiCRISPR-v2-Puro vector (Addgene, cat. no. 52961) as previously described⁵². The plasmid was co-transfected into 293T cells along with lentiviral packaging plasmids. Following a 72 h incubation, lentiviral supernatants were gathered and filtered for subsequent cell infection. The cells exhibiting a successful *Rab27a* KO were selected through the use of 2 $\mu\text{g ml}^{-1}$ puromycin. Monoclonal KO cells were then isolated utilizing a limited dilution technique and confirmed via western blot analysis.

Collection of sEVs

To collect sEVs, tumour cells underwent a 48–72 h incubation in RPMI 1640 or DMEM medium supplemented with 10% sEV-depleted foetal bovine serum. Subsequently, supernatants were gathered for sEV isolation employing a standard differential centrifugation protocol outlined in our prior studies⁵². Typically, the supernatants underwent centrifugation at 2,000g for 20 min at 4 °C, removing the pellet containing dead cells and cell debris. The resulting supernatants were then subjected to centrifugation at 16,500g for 40 min at 4 °C to pellet MVs. These supernatants were collected and further centrifuged at 100,000g for 2 h at 4 °C to isolate sEVs. The resuspended sEVs underwent additional

purification through centrifugation at 100,000g for 2 h and were subsequently resuspended in phosphate-buffered saline (PBS).

Evaluation of the uptake of LNPs or sEVs by MC38 cells

We first quantified the particle number of a sEV stock solution and a LNP (with similar size to sEVs) stock solution. A total of 5×10^9 sEVs or LNPs were labelled with the same amount of DiO and were added to MC38 *Rab27a* KO cells. After 24 h of incubation, the uptake of sEV-DiO or LNP-DiO by the cells was quantified using flow cytometry. To demonstrate if the addition of sEVs competing with LNPs or saturating the endocytosis capacity of tumour cells, MC38 *Rab27a* KO cells were cultured in 1 ml medium containing 5×10^9 sEVs or 5×10^9 LNPs. Then, to the cell culture medium, 5×10^9 LNP-DiOs were added. After 24 h of incubation, the uptake of LNP-DiO by MC38 *Rab27a* KO cells was quantified using flow cytometry.

Determining the ratio of tumour cell-derived sEVs in the tumour tissue

We investigated the ratio of the tumour cell-derived sEVs in sEVs collected from tumour tissues. A total of 1×10^{10} of sEVs collected from MC38 cells and sEVs collected from the MC38 tumour tissue were incubated with the same dose of anti-EPCAM-PE antibody for 40 min. After that, free antibody was removed by centrifuge and the pellet was resuspended in 1 ml PBS. The fluorescence intensity of the mixture was measured using a fluorescence spectrophotometer. The ratio of tumour cell-derived sEVs (RI) was calculated as

$$RI = F2/F1,$$

where F1 represents the fluorescence intensity of the tumour cell-derived sEVs and F2 represents the fluorescence intensity of the tumour tissue-derived sEVs.

We further investigated the ratio of tumour cell-derived sEVs using a pull-down experiment. First, tumour cells were metabolically labelled with excess amount of azide group following a published method⁵³. This is to ensure that sEVs released from tumour cells are labelled with azide group. Azide-modified MC38 cells were used to construct the tumour model. After 14 days of tumour model construction, tumour tissues were collected and the total sEVs in the tumour tissue were isolated. Tumour-released sEVs were collected using a pull-down experiment described in Supplementary Fig. 15c. The total sEVs number and tumour-released sEVs number were determined using a nanoparticle tracking system, and the ratio of tumour cell-derived sEVs (R2) in all sEVs was calculated as

$$R2 = \text{number of bead pull-down sEVs} / \text{number of total sEVs}.$$

Flow cytometry

Liver, spleen or tumour tissues were sliced into $3 \times 3 \times 3$ mm cubes and enzymatically dissociated using 1 mg ml^{-1} type IV collagenase, 50 U ml^{-1} RNase and 50 U ml^{-1} DNase I for 40 min at 37 °C to obtain single-cell suspensions. The exclusion of dead cells was achieved using the Live/Dead Fixable Aqua Dead Cell Stain Kit (Thermo Fisher, cat. no. L34957). Cellular surface staining was conducted for 30 min on ice. Afterwards, the cells were washed with PBS three times, and the stained cells were analysed using flow cytometry (FACS LSR II). The data were analysed using FlowJo V10 software.

Synthesis of mRNAs

The codon-optimized sequences for firefly Luciferase, Cre recombinase, mouse phosphatase and tensin homologue (*Pten*), mutated mouse stimulator of interferon genes (*Sting*, R283S) and miR-122-*Sting* were cloned into an mRNA production plasmid. This plasmid, optimized with a 3' and 5' UTR and containing a 101 polyA tail, underwent

in vitro transcription in the presence of *N*1-methyl pseudouridine modified nucleoside. The transcripts were co-transcriptionally capped using CleanCap technology from TriLink and then cellulose purified to eliminate double-stranded RNAs. Following purification, the mRNAs were precipitated in ethanol, washed, resuspended in nuclease-free water and subjected to quality control measures such as electrophoresis, dot blot and endotoxin content analysis. Subsequently, all mRNAs were stored at -80°C until their use.

Preparation of LNPs, gold nanoparticles, silica nanoparticles, PLGA nanoparticles, PS nanoparticles and liposomes

DLin-MC3-DMA, 1,2-distearoyl-*sn*-glycero-3-phosphocholine, cholesterol, and 1,2-dimyristoyl-*rac*-glycero-3-methoxypolyethylene glycol were combined at a molar ratio of 50/10/38.5/1.5 and dissolved in ethanol, while mRNA was dissolved in citrate buffer with a pH of 3. The lipid-containing ethanol phase was mixed with the aqueous phase using a microfluidic device at a flow rate ratio of 1:3. Subsequently, the resulting LNPs were dialysed against $1\times$ PBS in a dialysis cassette (molecular weight cut-off (MWCO) 20 kDa) for 2 h to eliminate ethanol and citrate buffer. The purified LNPs were then filtered through a $0.22\ \mu\text{m}$ membrane and stored at 4°C until needed. For experiments investigating the impact of tumour-derived extracellular vesicles on LNP cellular uptake, an mRNA encoding firefly luciferase was used for LNP formulation. In the synthesis of 93 nm and 125 nm LNPs, the ethanol phase and citrate buffer phase were mixed using a microfluidic chip device at a flow rate ratio of 1:3. The mixtures were left at room temperature for 30 or 90 min, respectively, before being added to dialysis cassettes (MWCO 20 kDa). For the DiR and/or DiD labelling process, 1 ml of LNPs were combined with $2\ \mu\text{l}$ of DiR or DiD dissolved in DMSO ($1\ \text{mg}\ \text{ml}^{-1}$) in a 1.5 ml tube. After pipette mixing and incubation at 25°C for 30 min, the mixture was loaded onto a 2 ml centrifugal filter device (MWCO 10 kDa) and washed with PBS three times to remove free DiR or DiD dye, ensuring that the dye remained attached to the LNPs.

Gold nanoparticles were produced using a seed-growth method, as detailed in prior reports⁵⁴. Initially, 15 nm gold nanoparticles were synthesized as seeds. A solution of $0.1\ \text{ml}\ \text{HAuCl}_4\cdot 3\text{H}_2\text{O}$ in 10 ml water was heated to boiling, followed by the addition of a $0.3\ \text{ml}$ sodium citrate solution. The mixture continued boiling for an additional 30 min and was allowed to cool to room temperature. To create 56.6 nm gold nanoparticles, $4.5\ \text{ml}$ of the 15 nm gold nanoparticle seed solution was combined with $4.88\ \text{ml}$ of $\text{HAuCl}_4\cdot 3\text{H}_2\text{O}$ solution ($10\ \text{mmol}\ \text{l}^{-1}$), and the mixture was diluted to 300 ml with ultrapure water. Subsequently, 200 ml of ascorbic acid solution (0.4 mM) was added drop-wise to the solution, resulting in the formation of 56.6 nm gold nanoparticles with a purple–red hue. A fluorescein isothiocyanate isomer I (FITC) modification approach was employed to prepare fluorescent gold nanoparticles, facilitating the examination of cellular uptake by cells.

The synthesis of silica nanoparticles was carried out according to a previously documented procedure⁵⁵. Pluronic F127 (0.025 g) was combined with *N*-cetyltrimethylammonium bromide (CTAB, 0.25 g) and dissolved in 120 ml of ultrapure water. Subsequently, $875\ \mu\text{l}$ of 2 M NaOH solution was introduced, and the temperature was set to 80°C . Following 15 min of stirring, $1.25\ \text{ml}$ of tetraethyl orthosilicate was added drop-wise to the mixture. The stirring continued for an additional 2 h until a blue–white colloidal solution was achieved. The resulting nanoparticles underwent filtration and were washed five times with methanol. For assessing cellular uptake of the nanoparticles, FITC was incorporated into the silica nanoparticles to impart fluorescence.

PLGA nanoparticles loaded with FITC were formulated using a nanoprecipitation approach⁵⁶. Specifically, 1 ml of a solution containing PLGA polymer and FITC in acetonitrile was swiftly introduced into 50 ml of PBS, leading to the generation of FITC-loaded PLGA nanoparticles. Subsequently, the nanoparticles underwent centrifugation and were subjected to three washes with PBS before being utilized.

The PS nanoparticles were labelled with amine functionalized rhodamine B using the 1-ethyl-3-(3-dimethylaminopropyl) carbodiimide (EDC) *N*-hydroxysuccinimide (NHS) chemistry reported previously⁵⁷.

Liposome nanoparticles were prepared employing a thin-film evaporation method. DPPC, cholesterol and DSPE-PEG-2000 in a molar ratio of 55:40:5 were dissolved in chloroform within a round-bottom flask. The organic solvent was evaporated overnight under reduced pressure (1 mbar). Subsequently, $1\times$ PBS was introduced to the lipid film, and the flask underwent sonication for 6 min. Finally, the particles were purified using centrifugal filters with a molecular weight cut-off of 10 kDa. For the creation of fluorescent liposomes, FITC-labelled DSPE-PEG-2000 was employed.

Characterization of nanoparticles

The size and polydispersity index of LNPs, gold nanoparticles, silica nanoparticles, PLGA nanoparticles, PS nanoparticles and liposomes were determined using a Malvern NanoZS 90.

Conjugation of LNP with sEV

Azide-modified LNPs were prepared using the protocol mentioned previously, except DOPE-azide was used to replace DOPE. Then, sEVs were labelled with DSPE-PEG-DBCO by incubating sEVs with 0.1% (w/w) DSPE-PEG-DBCO for 2 h. After that, free DSPE-PEG-DBCO was removed by dialysis (MWCO 20,000 Da), and sEV-DBCO was obtained. The LNP–sEV conjugation was prepared by mixing LNP-azide and sEV-DBCO (at a 1:1 particle number) and incubating in PBS (room temperature) for 1 h. The azide-DBCO click chemistry can induce fast conjugation of the two particles.

Generation of tumour spheroids

To establish a low attachment surface, 96-well round-bottom microplates were treated with 5% (v/v) Synperonic F-108 for 12 h. Subsequently, the F-108 solution was aspirated from each well, and the wells were washed three times with PBS before cell seeding. MC38 cells were then seeded into the coated wells at a density of 5,000 cells per well. The 96-well plates were placed in a cell incubator at 37°C , with a 5% CO_2 atmosphere and 95% air humidity. After an incubation period of 11 days, the tumour spheroids were collected for confocal experiments (Zeiss LSM710 equipped with a ZEN2010 software).

IVIS imaging

The IVIS scan was performed using a PerkinElmer Lumina III IVIS system. The images were acquired in the specified DiR channel (excitation 710 nm, emission 760 nm) using the auto exposure mode. The LivingImage 4.5 software's Auto region of interest (ROI) function was employed to quantify the fluorescence level. The figures were generated based on the average fluorescence intensity in each tissue.

Processing of single-cell RNA sequencing data

Data for single-cell RNA sequencing of healthy mouse liver was sourced from a previous publication⁵⁸. Mouse single-cell RNA sequencing datasets were downloaded from Gene Expression Omnibus (GSE109774). De-multiplexing of sequences from the NovaSeq was conducted using bcl2fastq version 2.19.0.316. Alignment of reads to the mm10plus genome was performed using STAR version 2.5.2b, with parameters TK. Gene counts were generated using HTSEQ version 0.6.1p1 with default settings, except for 'stranded', which was set to 'false', and 'mode', which was set to 'intersection-nonempty'. De-multiplexing and alignment were carried out using CellRanger version 2.0.1, provided by 10x Genomics, with default parameters.

The images in Supplementary Figs. 19, 20, 23 and 24b were adapted from The Human Protein Atlas based on a previous publication⁵⁹ for the following figures: Supplementary Fig. 19a, <https://www.proteinatlas.org/ENSG00000169896-ITGAM/tissue+cell+type/liver>; Supplementary Fig. 19b, <https://www.proteinatlas.org/>

ENSG00000169896-ITGAM/single+cell+type/liver; Supplementary Fig. 20a: <https://www.proteinatlas.org/ENSG00000160255-ITGB2/tissue+cell+type/liver>; Supplementary Fig. 20b, <https://www.proteinatlas.org/ENSG00000160255-ITGB2/single+cell+type/liver>; Supplementary Fig. 23, <https://www.proteinatlas.org/ENSG00000198053-SIRPA/tissue+cell+type/>; and Supplementary Fig. 24b, <https://www.proteinatlas.org/ENSG00000198053-SIRPA/pathology>.

Bulk RNA sequencing

MC38 tumour cells underwent a 24 h treatment with PBS, LNPs containing *siRab27a* and a control mRNA, LNPs containing a control siRNA and *Sting* mRNA and LNPs containing both *siRab27a* and *Sting* mRNA. Following treatment, the cells were collected, and the total RNA was extracted using the Invitrogen PureLink RNA Mini Kit. The extracted RNA was stored in a -80°C freezer until further use. Sequencing and data analysis were conducted by Novogen Co. The DESeq R package (version 1.20.0) was employed for analysing differentially expressed genes, and the Benjamini–Hochberg method was applied to adjust *P* values. Significantly differentially expressed genes were identified by setting a threshold of corrected *P* values at 0.05 and a \log_2 fold change of 1.

For sequencing of MC38 tumour tissue, mice bearing MC38 tumours were i.v. injected with PBS, LNPs containing *siRab27a* and a control mRNA, LNPs containing a control siRNA and *Sting* mRNA or LNPs containing both *siRab27a* and *Sting* mRNA. Intravenous injections were administered on days 8, 10, 12, 14 and 16, totalling five injections. On day 20, the mice were killed, and the tumour tissues from different treatment groups were collected. Total RNA was extracted from tumour tissues using the Invitrogen PureLink RNA Mini Kit, and the sequencing was performed by Novogen Co. using the methods mentioned above. Transcriptomics sequencing data are available from the Sequence Read Archive under accession code PRJNA1086632.

Immunofluorescence sample preparation

To prepare samples for immunofluorescence, a transcardiac perfusion was conducted by slowly injecting 50 ml of 10% neutral buffered formalin into the left ventricle. Subsequently, the organs and tumours from the mice were collected.

Statistics and reproducibility

Statistical analyses were conducted using GraphPad Prism 7.0 software. The error bars in the results represent the mean \pm standard deviation (s.d.). To assess statistical differences between two groups, a one-way analysis of variance (ANOVA) with Tukey's post hoc test was employed. For animal survival experiments, the *P* values were calculated using the Kaplan–Meier method-based log-rank test. All the data met the assumptions of the statistical tests used, including normality and equal variances, were formally tested before statistical differences were calculated. The sample size was not predetermined by a specific statistical method, and dosing groups were filled by randomly selecting from the same pool of animals for both in vitro and in vivo experiments. No data were excluded from the analyses. Importantly, all investigators were blinded to group allocation during the data collection and analysis processes.

Reporting summary

Further information on research design is available in the Nature Portfolio Reporting Summary linked to this article.

Data availability

All relevant data of this article are available within the paper and its Supplementary Information files. A dataset is provided with this paper. Transcriptomics sequencing data is available from the Sequence Read Archive under accession code PRJNA1086632. Mouse single-cell RNA sequencing datasets were downloaded from Gene Expression Omnibus (GSE109774). The images in Supplementary Figs. 19, 20, 23 and 24b were downloaded from The Human Protein Atlas (primary publication:

Uhlén M., Fagerberg L., Hallström B.M., et al. *Science*, 2015, 347(6220): 1260419.). Source data are provided with this paper.

References

- Zhang, W. et al. ICAM-1-mediated adhesion is a prerequisite for exosome-induced T cell suppression. *Dev. Cell* **57**, 329–343. e327 (2022).
- Gong, N. et al. In situ PEGylation of CAR T cells alleviates cytokine release syndrome and neurotoxicity. *Nat. Mater.* **22**, 1571–1580 (2023).
- Huo, S. et al. Superior penetration and retention behavior of 50 nm gold nanoparticles in tumour cell penetration and tumor retention of gold nanoparticles. *Cancer Res.* **73**, 319–330 (2013).
- Xing, L., Zheng, H., Cao, Y. & Che, S. Coordination polymer coated mesoporous silica nanoparticles for pH-responsive drug release. *Adv. Mater.* **24**, 6433–6437 (2012).
- Saad, W. S. & Prud'homme, R. K. Principles of nanoparticle formation by flash nanoprecipitation. *Nano Today* **11**, 212–227 (2016).
- Huo, S. et al. Ultrasmall gold nanoparticles as carriers for nucleus-based gene therapy due to size-dependent nuclear entry. *ACS Nano* **8**, 5852–5862 (2014).
- Consortium, T. M. et al. Single-cell transcriptomics of 20 mouse organs creates a *Tabula Muris*. *Nature* **562**, 367–372 (2018).
- Uhlén, M. et al. Tissue-based map of the human proteome. *Science* **347**, 1260419 (2015).

Acknowledgements

M.J.M. acknowledges support from a US National Institutes of Health (NIH) Director's New Innovator Award (DP2 TRO02776), a Burroughs Wellcome Fund Career Award at the Scientific Interface (CASI), a US National Science Foundation CAREER Award (CBET-2145491) and an American Cancer Society Research Scholar grant (RSG-22-122-01-ET). W.G. acknowledges supports from NIH R35 GM141832 and NCI P50 CA261608.

Author contributions

N.G., W.Z. M.-G.A., D.W., W.G. and M.J.M. conceived and designed the experiments. N.G., W.Z., M.-G.A., X.H., L.X., R.E.-M., G.Z., Z.Q., F.X., A.G.H., D.K. and J.X. performed the experiments, N.G., W.Z. L.X., X.H. and X.T. analysed the data. N.G., W.Z. M.-G.A., D.W., W.G. and M.J.M. wrote and edited the manuscript. J.L. and X.-J.L. were involved in discussion. D.W., W.G. and M.J.M. supervised the entire project. All authors discussed the results and commented on the manuscript.

Competing interests

N.G., M.J.M., W.Z. and W.G. have filed a patent (Lipid nanoparticle (LNP) compositions and methods for delivering therapeutic agents to tumour cells) related to this paper.

Additional information

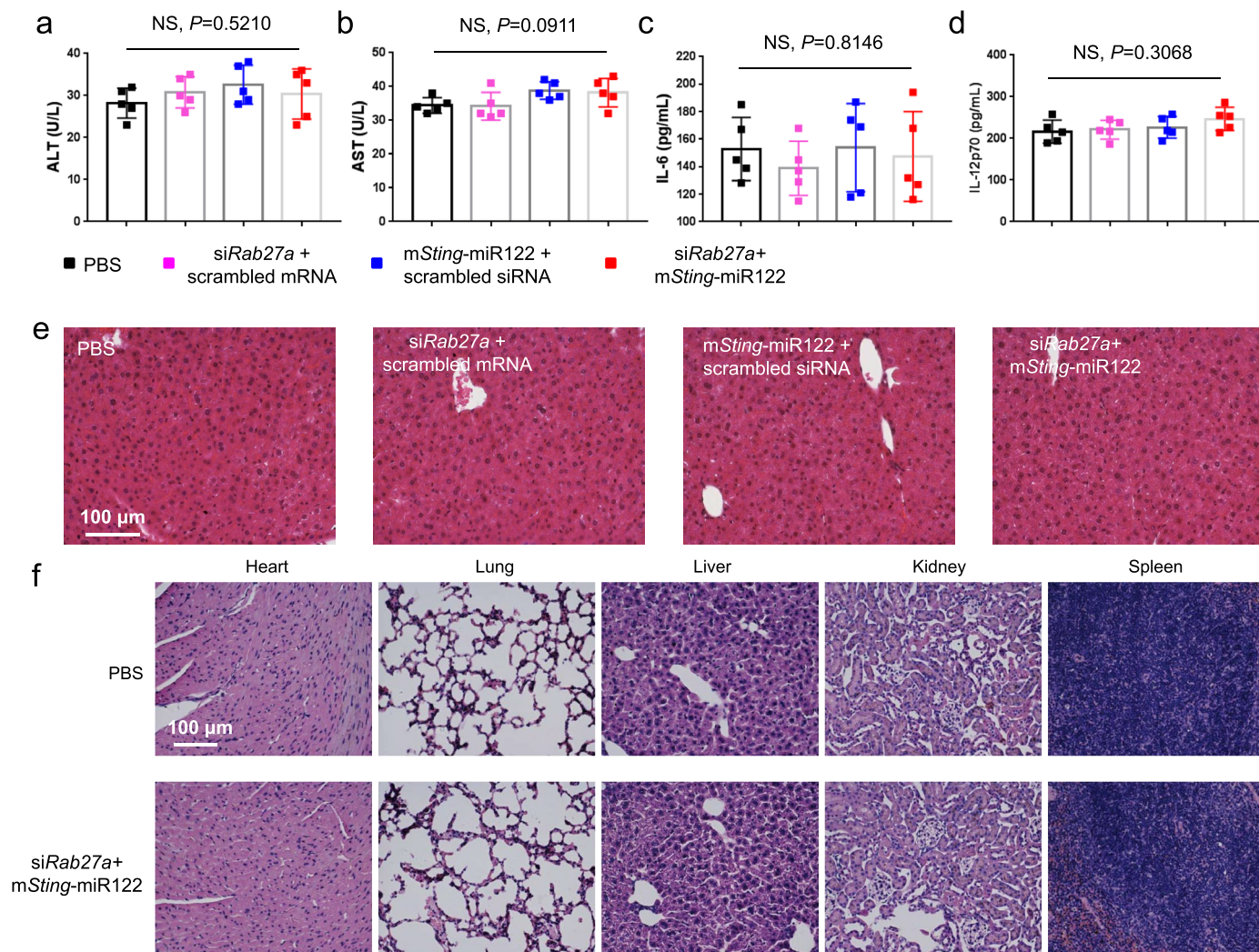
Extended data is available for this paper at <https://doi.org/10.1038/s41563-024-01961-6>.

Supplementary information The online version contains supplementary material available at <https://doi.org/10.1038/s41563-024-01961-6>.

Correspondence and requests for materials should be addressed to Drew Weissman, Wei Guo or Michael J. Mitchell.

Peer review information *Nature Materials* thanks Joao Conde and the other, anonymous, reviewer(s) for their contribution to the peer review of this work.

Reprints and permissions information is available at www.nature.com/reprints.



Extended Data Fig. 1 | LNPs delivering siRab27a and mSTING-miR-122 do not induce systemic toxicity. 1×10^6 MC38 cells were s.c. injected into the right flank of mice at day 0. At day 8, the tumour size reached 50 mm^3 . Mice were then treated with the following LNPs: 1) LNP co-encapsulating siRab27a and scrambled mRNA; 2) LNP co-encapsulating scrambled siRNA and mSTING-miR-122; or 3) LNP co-encapsulating siRab27a and mSTING-miR-122. These LNPs were i.v. injected (0.25 mg/kg) into mice at days 7, 9, 11, 13, and 15. PBS injections into mice at different time points were used as a control group. When tumour sizes in the PBS

group reached 1500 mm^3 (day 20), mice were euthanized and ALT (a), AST (b), IL-6 (c), and IL-12p70 (d) in mouse blood were measured. e, H&E staining of mouse livers collected from different groups. f, H&E staining of major mouse organs collected from the PBS group and the STING-miR-122 + siRab27a group at day 50. Data in a-d was shown as mean \pm s.d. ($n=5$ biologically independent samples). One-way ANOVA was used to determine statistical differences. e and f, Experiments were repeated independently 3 times with similar results.

Reporting Summary

Nature Portfolio wishes to improve the reproducibility of the work that we publish. This form provides structure for consistency and transparency in reporting. For further information on Nature Portfolio policies, see our [Editorial Policies](#) and the [Editorial Policy Checklist](#).

Statistics

For all statistical analyses, confirm that the following items are present in the figure legend, table legend, main text, or Methods section.

- | n/a | Confirmed |
|-------------------------------------|--|
| <input type="checkbox"/> | <input checked="" type="checkbox"/> The exact sample size (n) for each experimental group/condition, given as a discrete number and unit of measurement |
| <input type="checkbox"/> | <input checked="" type="checkbox"/> A statement on whether measurements were taken from distinct samples or whether the same sample was measured repeatedly |
| <input type="checkbox"/> | <input checked="" type="checkbox"/> The statistical test(s) used AND whether they are one- or two-sided
<i>Only common tests should be described solely by name; describe more complex techniques in the Methods section.</i> |
| <input type="checkbox"/> | <input checked="" type="checkbox"/> A description of all covariates tested |
| <input type="checkbox"/> | <input checked="" type="checkbox"/> A description of any assumptions or corrections, such as tests of normality and adjustment for multiple comparisons |
| <input type="checkbox"/> | <input checked="" type="checkbox"/> A full description of the statistical parameters including central tendency (e.g. means) or other basic estimates (e.g. regression coefficient) AND variation (e.g. standard deviation) or associated estimates of uncertainty (e.g. confidence intervals) |
| <input type="checkbox"/> | <input checked="" type="checkbox"/> For null hypothesis testing, the test statistic (e.g. F , t , r) with confidence intervals, effect sizes, degrees of freedom and P value noted
<i>Give P values as exact values whenever suitable.</i> |
| <input checked="" type="checkbox"/> | <input type="checkbox"/> For Bayesian analysis, information on the choice of priors and Markov chain Monte Carlo settings |
| <input checked="" type="checkbox"/> | <input type="checkbox"/> For hierarchical and complex designs, identification of the appropriate level for tests and full reporting of outcomes |
| <input checked="" type="checkbox"/> | <input type="checkbox"/> Estimates of effect sizes (e.g. Cohen's d , Pearson's r), indicating how they were calculated |

Our web collection on [statistics for biologists](#) contains articles on many of the points above.

Software and code

Policy information about [availability of computer code](#)

Data collection

Data analysis

For manuscripts utilizing custom algorithms or software that are central to the research but not yet described in published literature, software must be made available to editors and reviewers. We strongly encourage code deposition in a community repository (e.g. GitHub). See the Nature Portfolio [guidelines for submitting code & software](#) for further information.

Data

Policy information about [availability of data](#)

All manuscripts must include a [data availability statement](#). This statement should provide the following information, where applicable:

- Accession codes, unique identifiers, or web links for publicly available datasets
- A description of any restrictions on data availability
- For clinical datasets or third party data, please ensure that the statement adheres to our [policy](#)

The data that support the findings of this study are available within the paper and its supplementary Information files. A dataset is provided with this paper. RNA-seq data can be find xxxxx. The single-cell RNA sequencing data was download from a dataset (Gene Expression Omnibus, GSE109774). The data shown in Supplementary Figures 19, 20, 23, 24b are from The Human Protein Atlas (<https://www.proteinatlas.org/>)

Research involving human participants, their data, or biological material

Policy information about studies with [human participants or human data](#). See also policy information about [sex, gender \(identity/presentation\), and sexual orientation](#) and [race, ethnicity and racism](#).

Reporting on sex and gender	N/A
Reporting on race, ethnicity, or other socially relevant groupings	N/A
Population characteristics	N/A
Recruitment	N/A
Ethics oversight	N/A

Note that full information on the approval of the study protocol must also be provided in the manuscript.

Field-specific reporting

Please select the one below that is the best fit for your research. If you are not sure, read the appropriate sections before making your selection.

Life sciences Behavioural & social sciences Ecological, evolutionary & environmental sciences

For a reference copy of the document with all sections, see [nature.com/documents/nr-reporting-summary-flat.pdf](https://www.nature.com/documents/nr-reporting-summary-flat.pdf)

Life sciences study design

All studies must disclose on these points even when the disclosure is negative.

Sample size	No effect size was predetermined, but sample sizes employed in this study are consistent with previously published works (Li A W, Sobral M C, Badrinath S, et al. Nature materials, 2018, 17(6): 528-534; or Kuai R, Ochyl L J, Bahjat K S, et al. Nature materials, 2017, 16(4): 489-496.). For example, in vitro studies were repeated at least three times independently and in the in vivo experiments with 7-10 mice per group were performed.
Data exclusions	No animals and/or data were excluded.
Replication	All experiments were repeated for at least three times and experimental findings were reproducible.
Randomization	For animal experiments, dosing groups were filled by randomly selecting from the same pool of animals. Groups in all the in vitro and in vivo experiments were selected randomly.
Blinding	All the investigators were blinded to group allocation during data collection and analysis.

Reporting for specific materials, systems and methods

We require information from authors about some types of materials, experimental systems and methods used in many studies. Here, indicate whether each material, system or method listed is relevant to your study. If you are not sure if a list item applies to your research, read the appropriate section before selecting a response.

Materials & experimental systems

n/a	Involvement in the study
<input type="checkbox"/>	<input checked="" type="checkbox"/> Antibodies
<input type="checkbox"/>	<input checked="" type="checkbox"/> Eukaryotic cell lines
<input checked="" type="checkbox"/>	<input type="checkbox"/> Palaeontology and archaeology
<input type="checkbox"/>	<input checked="" type="checkbox"/> Animals and other organisms
<input checked="" type="checkbox"/>	<input type="checkbox"/> Clinical data
<input checked="" type="checkbox"/>	<input type="checkbox"/> Dual use research of concern
<input checked="" type="checkbox"/>	<input type="checkbox"/> Plants

Methods

n/a	Involvement in the study
<input checked="" type="checkbox"/>	<input type="checkbox"/> ChIP-seq
<input type="checkbox"/>	<input checked="" type="checkbox"/> Flow cytometry
<input checked="" type="checkbox"/>	<input type="checkbox"/> MRI-based neuroimaging

Antibodies

Antibodies used Anti-mouse F4/80 (Clone: BM8, Catalog: 123110, 1:100 dilution), anti-mouse CD19 (Clone: 6D5, catalog: 115538, 1:100 dilution),

Antibodies used	anti-mouse CD3 (Clone: OKT3, catalog: 317306, 1:100 dilution), anti-mouse CD31 (Clone: 390, catalog: 102410, 1:100 dilution), anti-mouse CD11c (Clone: N418, catalog: 117310, 1:100 dilution), anti-mouse PD-L1 (Clone: 10F.9G2, catalog: 124312, 1:100 dilution), anti-mouse EGFR (Clone: H11, catalog: MA5-13070, 1:100 dilution) were purchased from ThermoFisher. Anti-mouse EpCAM (Clone: VU-1D9, catalog: NBP2-33078PECY55, 1:100 dilution), was obtained from NOVUS Biologicals. Anti-mouse TRP1 antibody (Clone: EPR13063, catalog: ab178676, 1:100 dilution) was ordered from Abcam.
Validation	<p>All antibodies were verified by the supplier and each lot has been quality tested. All the antibodies used are from commercial sources and have been validated by the vendors. Validation data are available on the manufacturer's website.</p> <ol style="list-style-type: none"> 1. Anti-mouse F4/80-PE antibody has been validated to be used for flow analysis and mentioned species reactivity with mouse. (https://www.biolegend.com/en-us/products/pe-anti-mouse-f4-80-antibody-4068). 2. Anti-mouse CD19-BV421 antibody has been validated to be used for flow analysis and mentioned species reactivity with mouse. (https://www.biolegend.com/en-us/products/brilliant-violet-421-anti-mouse-cd19-antibody-7160). 3. Anti-mouse CD3-FITC antibody has been validated to be used for flow analysis and mentioned species reactivity with mouse. (https://www.biolegend.com/en-us/products/fitc-anti-human-cd3-antibody-3644). 4. Anti-mouse CD31-APC antibody has been validated to be used for flow analysis and mentioned species reactivity with mouse. (https://www.biolegend.com/en-us/products/apc-anti-mouse-cd31-antibody-118). 5. Anti-mouse CD11c-APC antibody has been validated to be used for flow analysis and mentioned species reactivity with mouse. (https://www.biolegend.com/en-us/products/apc-anti-mouse-cd11c-antibody-1813). 6. Anti-mouse CD274-APC antibody has been validated to be used for flow analysis and mentioned species reactivity with mouse. (https://www.biolegend.com/en-us/products/apc-anti-mouse-cd274-b7-h1-pd-l1-antibody-6655). 7. Anti-mouse anti-mouse EGFR antibody has been validated to be used for flow analysis and mentioned species reactivity with mouse. (https://www.thermofisher.com/antibody/product/EGFR-Antibody-clone-H11-Monoclonal/MA5-13070). 8. Anti-mouse EpCAM-PE/Cy5.5 antibody has been validated to be used for flow analysis and mentioned species reactivity with mouse. (https://www.novusbio.com/products/epcam-trop1-antibody-vu-1d9_nbp2-33078pecy55) 9. Anti-mouse TRP1 antibody has been validated to be used for flow analysis and mentioned species reactivity with mouse. (https://www.abcam.com/trp1-antibody-epr13063-ab178676.html).

Eukaryotic cell lines

Policy information about [cell lines and Sex and Gender in Research](#)

Cell line source(s)	The human melanoma cell lines WM9 were established in Meenhard Herlyn's laboratory (The Wistar Institute) (Catalog No. WM9-01-0001). The murine colon cancer cell line MC38 was purchased from from Sigma Aldrich (Catalog No. SCC172). Other cell lines including YUMM1.7 (catalog# CRL-3362), B16F10 (catalog# CRL-6475), NIH3T3 (catalog# CRL-1658), 293T (catalog#: CRL-3216) were originally obtained from ATCC.
Authentication	All the cell lines used were authenticated by STR profiling.
Mycoplasma contamination	All cell lines were tested for mycoplasma contamination. No mycoplasma contamination was found.
Commonly misidentified lines (See ICLAC register)	WM9, YUMM1.7, MC38, WM9, B16F10, NIH3T3 and 293T cell lines cell lines are not listed in the database.

Animals and other research organisms

Policy information about [studies involving animals; ARRIVE guidelines](#) recommended for reporting animal research, and [Sex and Gender in Research](#)

Laboratory animals	C57BL/6 mice and Ai14 mice (female, 6-8 weeks) were ordered from Jackson laboratory and housed in a specific-pathogen-free animal facility at ambient temperature (22 ± 2 °C), air humidity 40%–70% and 12-h dark/12-h light cycle.
Wild animals	No wild animal was used in this study.
Reporting on sex	Female mice were used in this study
Field-collected samples	The study did not involve samples collected from field.
Ethics oversight	All animal experiment protocols were reviewed and approved by the institutional animal care and use committee of the University of Pennsylvania.

Note that full information on the approval of the study protocol must also be provided in the manuscript.

Plants

Seed stocks	N/A
Novel plant genotypes	N/A
Authentication	N/A

Flow Cytometry

Plots

Confirm that:

- The axis labels state the marker and fluorochrome used (e.g. CD4-FITC).
- The axis scales are clearly visible. Include numbers along axes only for bottom left plot of group (a 'group' is an analysis of identical markers).
- All plots are contour plots with outliers or pseudocolor plots.
- A numerical value for number of cells or percentage (with statistics) is provided.

Methodology

Sample preparation	Mice blood was incubated with ammonium chloride buffer for erythrocyte lysis and washed with PBS. Single-cell suspensions were obtained by filtering through a 70 μ M cell strainer. Then the suspensions were stained with antibodies according to the manufacturer's protocols, and then analyzed by flow cytometry.
Instrument	BD LSR II
Software	FlowJo software package (Flowjo V10)
Cell population abundance	The absolute cells around 8000-10000 were analyzed for fluorescent intensity in the defined gate.
Gating strategy	In general, cells were first gated on FSC/SSC. Singlet cells were gated using FSC-H and FSC-A. Dead cells were then excluded and further surface and intracellular antigen gating was performed on the live cell population (Supplementary Figure 23).

- Tick this box to confirm that a figure exemplifying the gating strategy is provided in the Supplementary Information.